Local mechanical stimuli shape tissue growth in vertebrate joint morphogenesis

Ester Comellas[1,2,*], Johanna E Farkas[3], Giona Kleinberg[4], Katlyn Lloyd[4], Thomas Mueller[4], Timothy J Duerr[3], Jose J Muñoz[5,6,7], James R Monaghan[3,8], and Sandra J Shefelbine[2,4,*]

[1]Serra Húnter Fellow, Department of Physics, Laboratori de Càlcul Numeric (LaCàN), Universitat Politècnica de Catalunya (UPC), Barcelona, Spain
[2]Department of Mechanical and Industrial Engineering, Northeastern University, Boston, United States
[3]Department of Biology, Northeastern University, Boston, United States
[4]Department of Bioengineering, Northeastern University, Boston, United States
[5]Department of Mathematics, Laboratori de Càlcul Numeric (LaCàN), Universitat Politècnica de Catalunya (UPC), Barcelona, Spain
[6]Centre Internacional de Mètodes Numèrics en Enginyeria (CIMNE), Barcelona, Spain
[7]Institut de Matemàtiques de la UPC-BarcelonaTech (IMTech), Barcelona, Spain
[8]Institute for Chemical Imaging of Living Systems, Northeastern University, Boston, United States

* Authors for correspondance (ester.comellas@upc.edu, s.shefelbine@northeastern.edu)

Abstract

The correct formation of synovial joints is essential for proper motion throughout life. Movement-induced forces are critical to creating correctly shaped joints, but it is unclear how cells sense and respond to these mechanical cues. To determine how mechanical stimuli drive joint morphogenesis, we combined experiments on regenerating axolotl forelimbs with a poroelastic model of bone rudiment growth. Animals either regrew forelimbs normally (control) or were injected with a TRPV4 agonist to impair chondrocyte mechanosensitivity during joint morphogenesis. We quantified growth and shape in regrown humeri from whole mount light sheet fluorescence images of the regenerated limbs. Results revealed statistically significant differences in morphology and cell proliferation between the two groups, indicating that mechanical stimuli play a role in the shaping of the joint. Local tissue growth in our finite element model was dictated by a biological contribution, proportional to chondrocyte density, and a mechanical one, driven by fluid pore pressure dynamics. Computational predictions agreed with experimental outcomes, suggesting that interstitial pressure might promote local tissue growth. Predictive computational models informed by experimental findings allow us to explore potential physical mechanisms and regulatory dynamics involved in tissue growth to advance our understanding of the mechanobiology of joint morphogenesis.

Keywords: synovial joint development; TRPV4; cartilage mechanosensitivity; poroelasticity; continuum growth; finite element model

1 Background

The shape of a synovial joint is critical to its functionality in movement and locomotion. Joint morphogenesis in the developing vertebrate limb bud follows a well-known sequence of events [1]. First, the mesenchymal cells forming the early limb bud differentiate into chondrocytes, except for those in the interzone, where the future joint will appear. Through a process known as cavitation, the skeletal rudiments are physically separated and the synovial cavity is formed. After cavitation, chondrocyte proliferation and matrix production in the rudiment result in growth and final joint shape. Movement-induced mechanical stimuli condition the correct formation of joints throughout this morphogenetic stage [2,3]. Yet, how motion and biophysical forces influence joint shape is not fully understood to date [4,5]. Insights into how chondrocytes proliferate and regulate joint shape in response to mechanical stimuli during morphogenesis has application in the study and treatment of joint deformities [5].

Animal studies using immobilised chicks [6–10], reduced-muscle and absent-muscle mice [11–13], and paralysed zebrafish larvae [14] have shown that reduced and restricted muscle contractions during embryonic development results in skeletal abnormalities, including alterations in joint shape. Elucidating the role of motion in joint development is challenging in animal models that develop in ovo or in utero [3]. An animal model that allows rigorous control of the biophysical environment during joint morphogenesis will further our understanding of how mechanical stimuli are linked to cell proliferation and tissue growth. Axolotl salamanders (*Ambystoma mexicanum*) regenerate limbs throughout life by recapitulating developmental processes. Regenerating axolotl limbs undergo stereotypical patterns of gene expression and cell differentiation that resemble mammalian joint development [15, 16]. Their limbs are morphologically similar to human limbs, with elbow joints comparable in cellular composition and skeletal structure to mammalian synovial joints [17, 18].

Joint morphogenesis in vertebrates is driven by the proliferation and subsequent hypertrophy of chondrocytes that form the bone rudiments. Chondrocytes respond to mechanical stimuli such as changes in osmotic pressure, cellular stretch, or fluid shear [19]. Ion channels, integrin signalling, and the primary cilia are all known mechanosensors that initiate intracellular signalling cascades ultimately resulting in the transcription, translation, and/or molecular synthesis that leads to cartilage tissue growth [19–21]. In vitro studies have shown that the transient receptor potential vanilloid 4 (TRPV4) channel is possibly a key transducer of biophysical stimuli to regulate cartilage extracellular matrix production [22–24]. TRPV4 activation in chondrocytes has been linked to osmolarity changes in in vitro studies [25, 26]. Recent studies have shown it also responds to physiologic levels of strain loading [27, 28], although there is also evidence to the contrary [29, 30].

To tease out the specific mechanical stimuli influencing joint shape, computational models can help decipher the role of biophysical stimuli in tissue growth and joint morphogenesis. Techniques like finite element analysis (FEA) are specially suited to studying the mechanics of morphogenesis. They allow for the quantitative, unbiased testing of the biophysical mechanisms that might be regulating and controlling morphogenesis [31, 32]. A few studies have used FEA to examine how changes in mechanical loading affect joint morphogenesis [33–36]. These models demonstrated shape changes based on generic joint shapes and idealised loading conditions in two dimensions. The computational models assume that dynamic hydrostatic compression promotes cartilage growth, which is in line with experimental studies that have shown an increase in matrix production with cyclic compression [37–41]. Yet, these numerical studies use a static approximation via linear elasticity. As such, they are unable to intrinsically capture the effects of dynamic loading on a poroelastic medium, including the fluid flow and pore pressure to which cells likely respond. To better comprehend how local mechanical stimuli drives the shaping of the joint, we incorporate a fluid component in our model to account for the dynamic changes in pressure and

velocity of extracellular fluid present in cartilage.

The goal of this study is to determine the effect of limb motion on joint morphology, and identify potential mechanisms by which mechanical loading is translated into chondrocyte proliferation and unequal tissue growth that results in joint shape. Opening the TRPV4 channel in vivo in axolotls that were regrowing their forelimbs rendered the chondrocytes unable to sense and respond to changes in mechanical stimuli during the joint morphogenesis process [42, 43]. Then, using a technique for the three-dimensional visualisation of macromolecule synthesis [44] we quantified cell proliferation and joint shape for the mechanosensitively-impaired and the healthy joint formation cases. In this way we identified the effect of dynamic local mechanical stimuli on cell proliferation, tissue growth and joint morphogenesis. To test our hypothesis, we developed a three-dimensional biphasic poroelastic model in which growth of the solid component is driven by both morphogenetic factors and mechanical stimuli induced by dynamic local loading conditions. Experiments on regenerating axolotl forelimbs with and without the ability to respond to mechanical cues show that local mechanical stimuli indeed promote chondrogenesis and determine joint morphology. Our poroelastic growth model of joint morphogenesis allows the exploration of the physical stimuli that contribute to tissue growth and, in this way, dictate the shape of the grown joint. Combining both, i.e. using experimental data to inform our computational modelling and comparing predicted computational outcomes to observed experimental results, we can confidently begin to unravel the role of mechanics in vertebrate joint formation.

2 Axolotl experiments

To determine the effect of local mechanical stimuli on tissue growth during joint morphogenesis we restricted the ability of cells to respond to mechanical stimuli in regrowing axolotl forelimbs using the TRPV4 agonist GSK1016790A. Most known genetic disfunctions of the TRPV4 channel resulting in skeletal dysplasias are related to a gain of function [45, 46]. The lack of regulation of intracellular calcium ions induced by the chemical activation of TRPV4 channels means that the chondrocytes lose their mechanosensitivity and are effectively unable to detect and respond to mechanical stimuli [42, 43].

We quantified the shape and growth of the fully-formed elbows through a detailed analysis of the humerus bone rudiments. Comparison of normally-regrown limbs (control group) with those that were mechanosensitively-impaired (GSK101 group) during the joint morphogenesis stage reveals statistically significant differences in bone rudiment shape and cell proliferation levels.

2.1 Experimental Methods

Larval animals (3-5 cm) were bilaterally amputated just proximal to the elbow joint. GSK1016790A was reconstituted in dimethyl sulfoxide (DMSO) and injected intraperitoneally at 50 µg/kg at 22 days post amputation (dpa, n=6). Control animals (n=6) were injected with 50 µg/kg DMSO. Injections were repeated at 48-hour intervals. At 32 dpa, all animals were injected intraperitoneally with 5-Ethynyl-2'-deoxyuridine (EdU) and L-Azidohomoalanine (AHA). Limbs were collected 18 hours later, fixed and stained.

We imaged nascent macromolecule synthesis in the regenerated forelimbs with light sheet fluorescence microscopy (LSFM) following the whole-mount click-it-based technique in Duerr et al. [44]. We selected EdU to visualise DNA synthesis, which allowed quantification of cell proliferation. AHA enabled visualising chondrocyte protein translation, i.e. most likely extracellular matrix, which provided a well-defined outline of the bone rudiment's perichondria. Quantification of 3D shape was then possible through the analysis of the humerus outline.

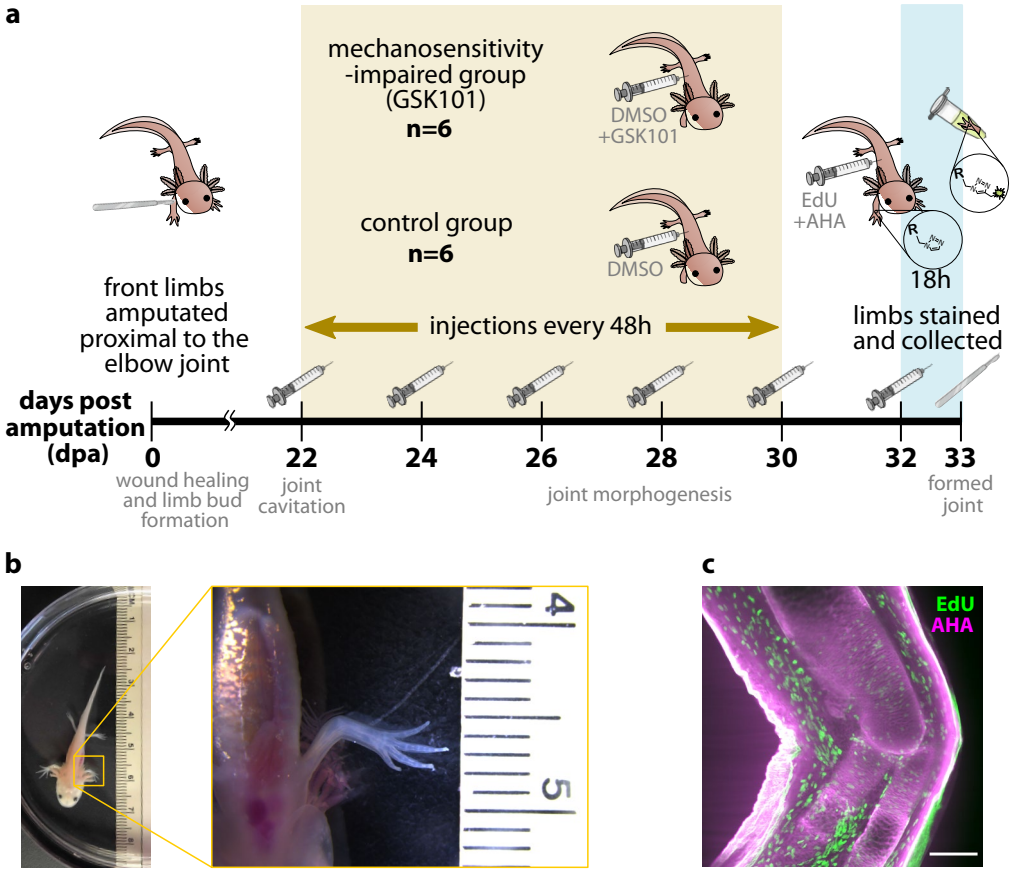

Figure 1: (a) Timeline of the experiments. Created with images from BioRender.com and smart.servier.com. (b) Animals 3-5 cm in size were used, similar to the one shown here. Both the image of the whole animal as well as the close-up of a forelimb include a ruler in cm. (c) Axolotl forelimbs were imaged following the whole-mount click-it based visualisation technique in [44] to obtain an image stack of the regenerated elbow joint. A central slice of a 3D image stack is shown here. The scale bar length represents 300 µm.

Figure 1a illustrates the timeline of the experiments and Figure 1b shows an example of the animal size used. Injections started at 22 dpa, which is roughly when joint cavitation occurs in regenerating limbs in 3-5-cm-sized animals, and continued throughout the joint morphogenesis stage of the joint formation process until 30 dpa. Figure 1c shows a central slice of a 3D image stack obtained for an exemplary control elbow. All images were acquired using a Zeiss light sheet Z.1 microscope paired with Zen software. In-plane pixel resolution of the image is 0.9154 µm and slices are 4.9454 µm apart. The file size containing both the EdU and AHA channels is about 3 GB.

2.2 Data Analysis

Figure 2 outlines the light sheet image processing pipeline followed to analyse the shape of each humerus and count the proliferating cells within the bone rudiment. First, the 3D image stack was cropped and rotated to roughly orient the proximo-distal (P-D) axis of the humerus in the vertical direction (Figure 2a). The AHA channel was used to extract the bone rudiment shapes (Figure 2b) through segmentation of the humerus, radius, and ulna (Figure 2c). The data for the posterior alignment of the limb in 3D space was obtained (Figure 2d) from the humerus and ulna masks using the Fiji plugin BoneJ [47].

To systematically analyse the humerus shape, we first aligned the segmented bone rudiment

surfaces to a standard orientation (Figure 2e). The alignment process included mirroring of right limbs so that all limbs had the medial and lateral epicondyles in the same relative position in space. We fitted a cylinder to the humerus surface and placed a hemisphere on top. This reference surface was then shifted vertically upwards until it was tangent to the distal end of the humerus surface (Figure 2f, left). The perpendicular distance from the reference surface to the humerus surface was mapped onto the reference surface. Both the mapped distance and the reference surface dimensions were normalized with the fitted cylinder diameter to account for animals of different size (Figure 2f, centre). We flattened out the mapped values (unwrapping the cylinder and hemisphere) to obtain a 2D standardised humerus surface representation, where red indicates a protuberance (the epicondyles) and blue shows the concavities of the original 3D surface (Figure 2f, right). Next, we computed a contour map from the 2D surface map (Figure 2g, left) and extracted the data within the closed contours of 0.2 (Figure 2g, right), which correspond to the normalized humerus epicondyles. Finally, we quantified their shape through computation of the normalized area and normalized volume within the extracted contours (Figure 2h). Once all limbs had been processed, we aligned the 2D surface maps based on the position of the medial epicondyle centroids. Then, we computed a mean 2D surface map of the control and GSK101 groups. These allowed reconstructing a mean 3D humerus surface for each group.

Proliferating cells were quantified by analysing the EdU channel (Figure 2i). We manually generated a small training set to train the deep learning algorithm Startdist3D [48], which was used to identify the stained cell nuclei in the 3D image stack. Memory limitations in Stardist3D required splitting the original image stack into smaller substacks for processing (Figure 2j). The Fiji plugin 3D Objects Counter [49] was used on the cell nuclei masks produced by Stardist3D to identify proliferating cell positions and volumes. The data was then regrouped and the whole set was masked with the humerus bone outline obtained in Figure 2c. The data from Figure 2d was used to align the cell nuclei in 3D space (Figure 2k, left). Outliers were removed based on cell volume and we used a fixed-length cut-off to ensure quantification of cell proliferation was performed in an equivalent humerus volume across different limbs (Figure 2k, right).

Figure 2 ***(following page)*****:** Workflow of the experimental data analysis using an exemplary control limb. (a) Each 3D image stack was cropped around the elbow joint and rotated to vertically align the proximo-distal (P-D) axis of the humerus. (b) The AHA staining in (a) allowed for segmentation of the bone rudiments, producing (c) the masks of the radius, ulna and humerus. (d) The Fiji plugin BoneJ provided data for limb alignment, based on the principal axes of the humerus and ulna bone rudiments. The minimum principal axis computed by BoneJ corresponded with the proximo-distal longitudinal axis of the bone rudiment. (e) Using data from (d), the surfaces in (c) were aligned in 3D space using Matlab. (f) The aligned humerus from (e) was mapped onto a reference surface and normalized with the fitted cylinder diameter to create a 2D representation of the humerus' 3D surface. (g) The representation of the lateral and medial epicondyles were extracted and (h) systematically quantified for each limb. (i) The EdU staining in (a) was used to identify the proliferating cell nuclei within the humerus bone rudiment. (j) Stardist was trained with a custom-made dataset. Substacks of the original 3D image were fed to the algorithm, which provided the corresponding cell nuclei segmentations. (k) Substacks of cell nuclei segmentations were re-grouped, nuclei within the humerus were extracted using the corresponding mask from (c) and aligned in space using data from (d). After removal of outliers, the position of each nucleus' centre of mass and volume was plotted in 3D space. Total number of cells were counted within an equal volume among all humeri.

Initial data

Part 1: bone rudiment segmentation and alignment data

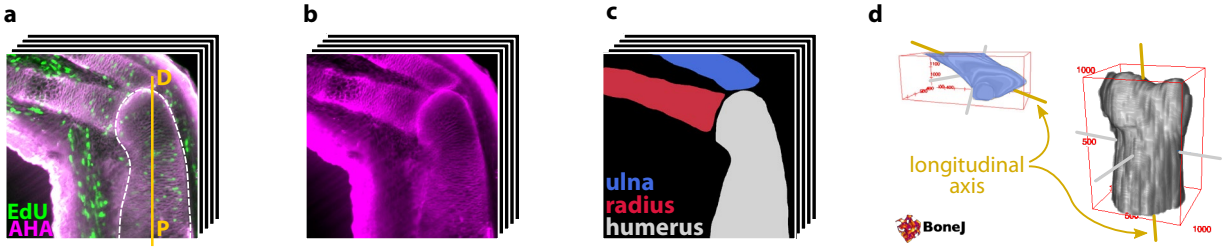

rotated and cropped stack

extract organ-level data from AHA channel

masked bone rudiments

3D limb alignment data

Part 2: humerus 3D shape analysis

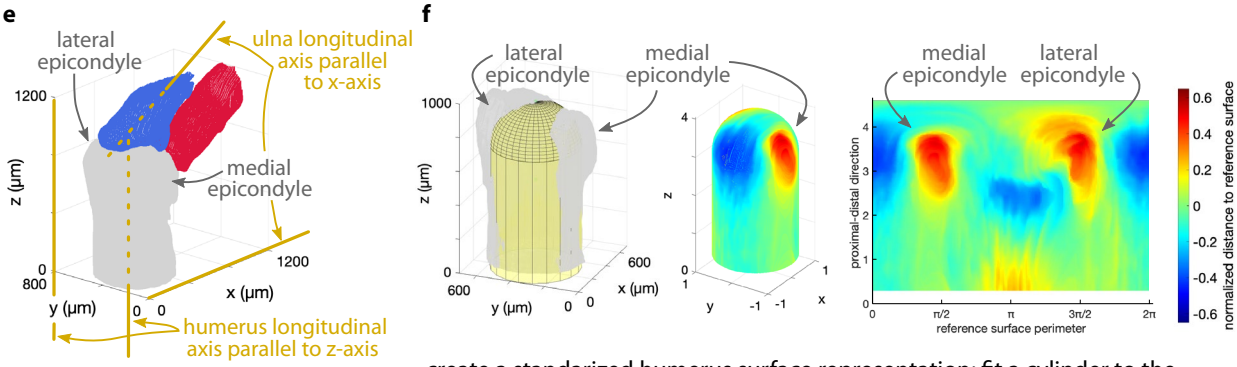

align limbs, including mirroring of right limbs

create a standarized humerus surface representation: fit a cylinder to the humerus shaft and add a hemispherical cap on top; map the distance to the humerus surface onto this reference surface and normalize the mapping; flatten out the surface map

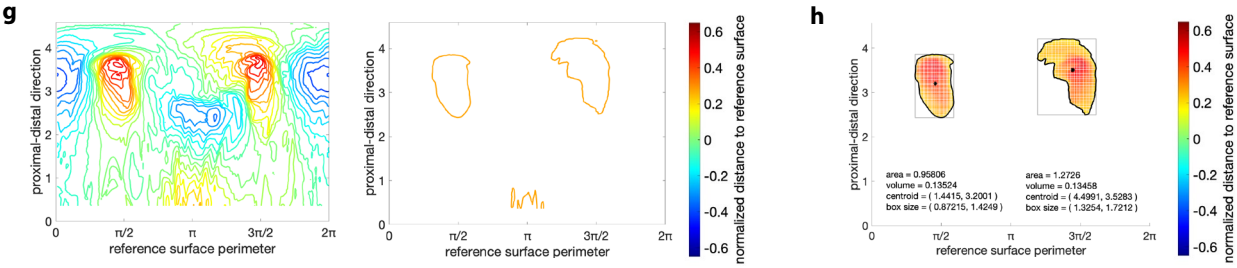

extract epicondyle data: compute contour map; extract information contained within closed contours of 0.2

quantify epicondyle shapes: normalized areas and volumes

Part 3: humerus 3D proliferating cell count

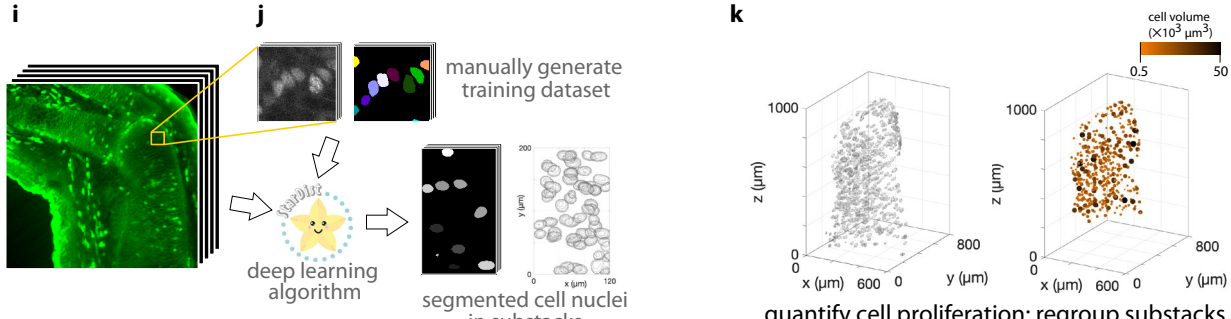

extract cell-level data from EdU channel

segment stained cell nuclei in substacks of original image

quantify cell proliferation: regroup substacks, mask detected cells within humerus and align using data from Part 1; remove outliers based on cell volume and use a fixed-length cut-off

To quantify shape and growth differences between the control and GSK101-treated limbs we focused on the following measurements: (i) the total count of EdU-positive cell nuclei (Figure 2k, right); (ii) the diameter of the cylinder fitted to each humerus shaft used in the generation of the reference surface (Figure 2f, left); and (iii) normalized volume and area of both the lateral and medial epicondyles (Figure 2h). We grouped all limb results for each measurement and ran a Shapiro-Wilk normality test. Except for the proliferating cell count, all other data measurements were normally distributed. We then performed a one-way ANOVA to check for statistically significant differences between the control and GSK101 experimental groups of normally-distributed data. The proliferating cell count p-value was obtained using a Kruskal-Wallis test.

The workflow was implemented using a combination of Fiji [50], the ZeroCostDL4Mic implementation of Startdist3D [51] and a customised code in Matlab [52]. A detailed description of the process and the scripts created to implement it are provided as Supplementary Material.

2.3 Experimental Results

Figure 3a provides the results of the statistical analysis on the measures obtained following the data processing pipeline summarized in Figure 2. Our results show significant differences in growth and shape between the humeri of the control group and the mechanosensitively-impaired (GSK101) group. The mean value of the proliferating cell count in the control group is fourfold that of the GSK101 group (p-value$<$0.001). A central slice of each EdU-stained humeri is provided in Figure 3b. The cell nuclei identified in two representative humeri of each group are plotted in 3D (Figure 3c), showing the striking difference in chondrocyte proliferation between the control and GSK101 groups. However, as shown in Figure 3a, the diameter of the cylinders fitted to the humeri shaft is similar for the two groups. Regarding humeri shape, the normalized volumes of both medial and lateral epicondyles are larger for the control group than the GSK101 group (p-value$=$0.005 and $<$0.001, respectively). The normalized areas of the lateral epicondyles in the control group are also larger (p-value$<$0.001), while no significant difference was found for the normalized areas of the medial epicondyles. Figure 3d provides a visual representation of these differences through the reconstruction of a mean humerus surface for the control and GSK101 groups. Individual 2D surface maps of each limb are provided in Appendix A.2. The mean humerus 3D surfaces, reconstructed from the 2D maps, are overlaid for comparison (Figure 3e).

Figure 3 ***(following page)*****:** Processed experimental results. (a) Results of the statistical analysis on the data points obtained following the methodology outlined in Figure 2. All data was normally distributed (Shapiro-Wilk test), except for the proliferating cell number. We performed a Kruskal-Wallis test for the latter, and a one-way ANOVA for all other measures to obtain the p-values. (b) EdU-stained masked humeri. The maximum intensity projection of 20 central slices in each humerus is shown. All images have the same 200 µm scale bar (top right). The two control humeri marked with a red cross were excluded from the 3D shape analysis because they were too short to be aligned with the methodology summarized in Figure 2. (c) The 3D cell nuclei positions for a representative humerus of each group (marked with an asterisk in b) are shown. (d) Mean 2D surface maps for the control and GSK101 groups. The corresponding mean normalized humerus surface (in grey) is recovered for both groups. (e) The mean humerus surface for the control and GSK101 groups are aligned for comparison. A diameter of 450 µm is used for both.

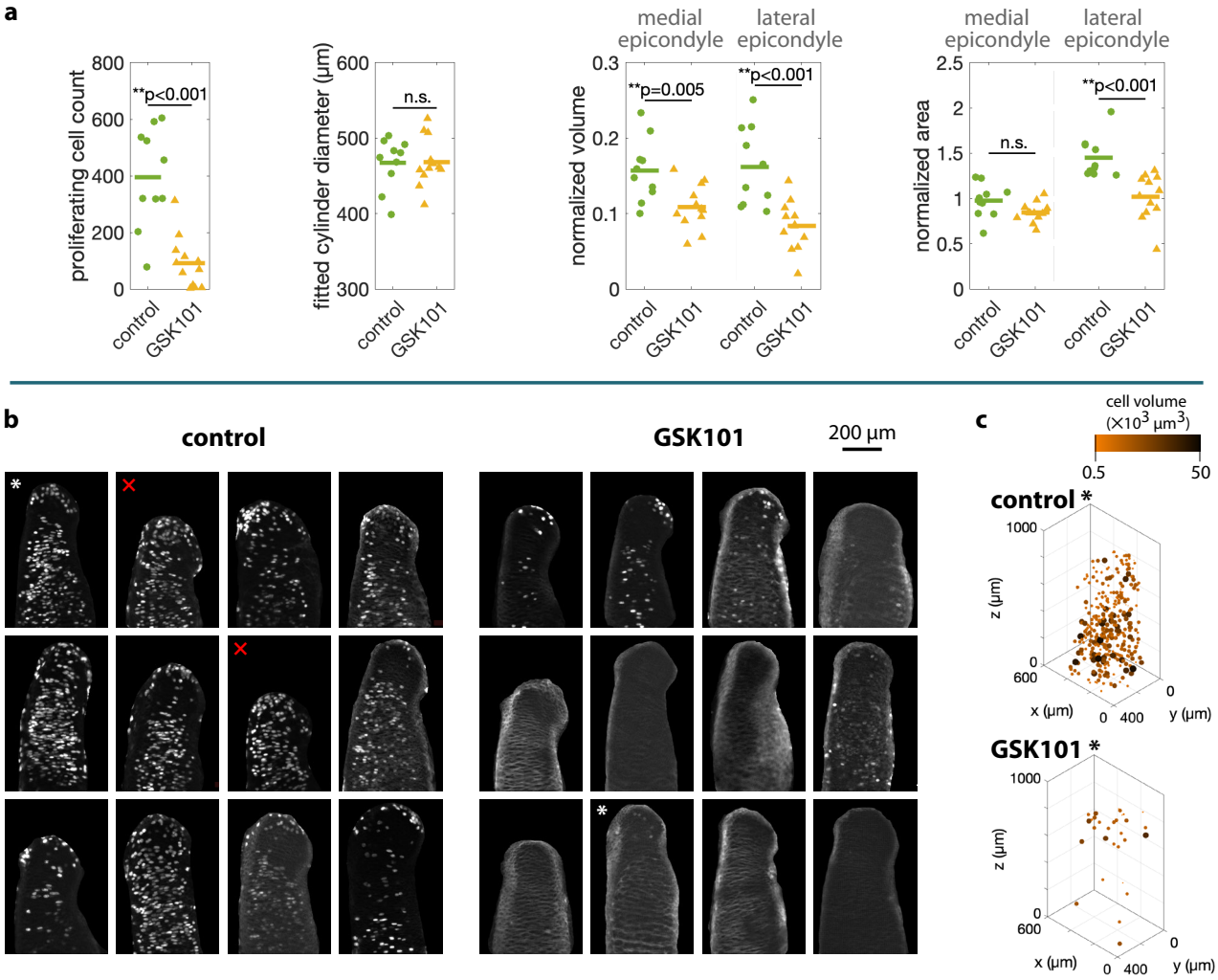

3 Computational modelling

We created an experimentally-informed finite element model of a developing humerus with the aim of exploring potential movement-induced mechanical stimuli as drivers of tissue growth. The humerus tissue was modeled as a biphasic poroelastic material, where growth of the solid component was hypothesized to be driven by a biological component and a local dynamic mechanical stimulus. A growth model based on local changes in fluid pressure induced by an elbow flexion-extension loading cycle predicted a final humerus morphology that resembled our experimental observations of the control group. When the mechanically-driven growth component was removed, shape prediction was in accordance with the experimental observations of the mechanosensitively-impaired GSK101 group.

3.1 Poroelastic framework with continuum growth

Cartilage tissue has a water content of roughly 80% by volume of tissue mass [53]. The mechanism for transduction of mechanical forces in tissues is not completely understood, but fluid flow is known to play an important role [19]. Poroelastic theory is commonly used in finite element models of cartilage response to loading [54–57] because it can explicitly capture the fluid flow effects.

The biphasic approach defines tissue as a mixture of an elastic solid skeleton with free-flowing fluid circulating within its pores. In cartilage, the fluid can be assimilated to the interstitial fluid in the tissue, i.e. water and dissolved ions, growth factors and other molecular components. The solid component represents the proteoglycans and collagen of the extracellular matrix (ECM) and chondrocytes. Chondrocyte proliferation and ECM production in cartilage can then be modeled through continuum growth of this solid phase. To our best of knowledge, this is the first computational model of cartilage tissue growth using biphasic theory. Unlike previous models of joint morphogenesis [33–36], the effect of fluid flow is explicitly incorporated in our simulations, allowing us to better test our hypothesis that local dynamic mechanical stimuli are the drivers of tissue growth, and ultimately determine joint shape.

3.2 Numerical framework for poroelasticity

The biphasic nature of cartilage tissue is modeled using poroelastic theory. The deformation of the solid component is characterized by its displacements $\boldsymbol{u}_S$ while the fluid behaviour is defined by the pore pressure p. The governing equations required to solve the problem for the two unknowns, $\boldsymbol{u}_S$ and p, are the linear momentum and mass balance equations. These introduce the constitutive equations of the solid and fluid components, respectively. The solid behaviour is characterized by the Kirchhoff stress tensor $\boldsymbol{\tau}$ while the fluid flow is defined by the seepage velocity $\boldsymbol{w}$, which is the relative velocity of the fluid with respect to the deforming solid. For simplicity, we considered a neo-Hookean hyperelastic model for the solid part and a Darcy-like law for the fluid one. An overview of the mathematical details of the poroelastic formulation is provided in Appendix B.

3.3 Growth model of the solid component

Tissue growth is modelled via the multiplicative decomposition of the deformation gradient tensor $\boldsymbol{F}$ that characterizes the solid component deformations, which include both the deformation and the growth due to loading (Figure 4). For simplicity, the growth tensor is assumed to be volumetric and proportional to the growth stretch ϑ. Following a common approach in the field [32–34,58] we

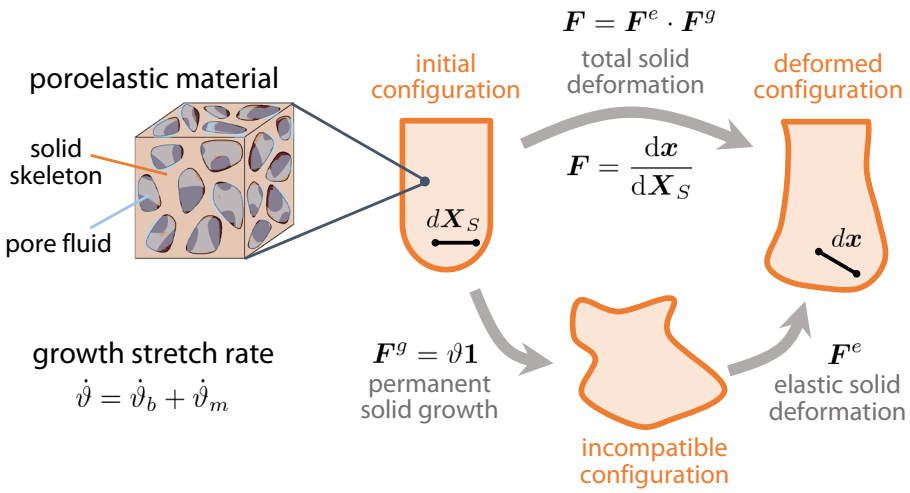

Figure 4: Continuum growth in the computational model is based on the multiplicative decomposition of the deformation gradient tensor $\boldsymbol{F}$ that characterizes the solid component of the poroelastic material. $\boldsymbol{F}$ maps a vector from the initial or reference configuration $d\boldsymbol{X}_S$ into a new position after deformation in the current configuration $d\boldsymbol{x}$. It is split into an elastic deformation gradient tensor $\boldsymbol{F}^e$ and a growth tensor $\boldsymbol{F}^g$. For simplicity, growth is assumed to be volumetric and proportional to the growth stretch variable ϑ, whose rate is the sum of a biological contribution $\dot{\vartheta}_b$ and mechanical contribution $\dot{\vartheta}_m$.

consider growth rate to be a sum of biological and mechanical contributions, denoted respectively by $\dot{\vartheta}_b$ and $\dot{\vartheta}_m$.

The biological contribution represents the intrinsic morphogenetic biological factors that globally mediate tissue growth. Similar to past studies of joint morphogenesis [33, 34], we assumed it is proportional to chondrocyte density in the bone rudiments. However, unlike these studies, our experimental measurements of chondrocyte density in a regenerating axolotl humerus revealed an approximately constant value throughout the bone rudiment (Figure B.1). Therefore, we defined a constant biological growth stretch rate $\dot{\vartheta}_b$ in time and space, within the humerus geometry and throughout the whole simulation time period.

The mechanical contribution is a function of the selected mechanical stimulus locally driving tissue growth. Mechanical loading is known to modulate the synthesis of ECM in chondrocytes. Collagen and aggrecan production, the main components of ECM in cartilage, depends on the magnitude, duration and type of loading. In particular, in vitro experiments have shown that cyclic compression promotes ECM production while static loading either has no effect on collagen and aggrecan levels, or inhibits cartilage growth [37–41]. Based on this experimental evidence, past models considered (compressive) hydrostatic stress as a driver of mechanical growth [33–35]. Even with the simplifying assumptions considered and generic joint shapes used, Giorgi et al. [34] could predict anatomically recognisable joint shapes based on different starting joint configuration and applied movements. Their results indicate that hydrostatic stress could be mediating tissue growth in response to mechanical load. However, models to date used a single-phase elastic material to represent tissue behaviour and, hence, were unable to inherently distinguish between dynamic and static loading effects. Our poroelastic model overcomes this limitation and, for the first time, we are able to define mechanical growth proportional to a dynamic variable linked to the movement-induced fluid flow. We selected pore pressure of the fluid component, a hydrostatic measure akin to the hydrostatic stress used in past models, as the mechanical stimulus. Fluid pressure is the simplest stimulus available in our model to begin to explore how dynamic external loading could be shaping the growing joint.

The details of the growth model and its numerical implementation are provided in Appendix B.

3.4 Finite element implementation

The discretized governing equations and continuum growth model were implemented in the open source finite element library `deal.II` [59]. The code used in this study is an extension of the poro-viscoelastic numerical framework provided in Comellas et al. [60] and available in the `deal.II` code gallery website. Growth was implemented following the algorithm described in Appendix B.3. Quadratic shape functions were used to approximate the solid displacements, linear shape functions were used to approximate the pore pressure, and a quadrature of order 3 was considered in all the simulations.

3.5 A finite element model of joint morphogenesis

We generated a finite element (FE) model of a generic humerus bone rudiment after cavitation with the goal of predicting the grown humerus shape at the end of the joint morphogenesis stage. Given that our model is a tool to probe potential mechanisms of load mechanotransduction in joint morphogenesis, we strove to keep its parameters as generic as possible.

The geometry and loading conditions were informed by experimental data from a regenerating axolotl forelimb just after joint cavitation. We segmented the bone rudiment shapes of a normally-regenerating forelimb at 17 dpa in a 3-cm-sized animal (Figure 5a).

A mesh was generated based on the smoothed-out surfaced of the segmented humerus with a total of 512 hexahedral elements. We scaled the geometry size to achieve a cross-sectional humerus size closer to the values identified in our experiments. Meshing of the geometry inevitably entails a slight loss of surface detail. We computed and visually compared the 2D surface maps of both the segmented geometry and the meshed geometry (Figure 5b) following a procedure analogous to the one used in the humerus 3D shape analysis shown in Figure 2f. Comparison of 2D surface maps confirmed that the meshed surface retained the main characteristics of the original humerus. Interestingly, the lateral epicondyle was not present yet at this stage of joint formation for the segmented forelimb, while the medial epicondyle seemed to be already well formed.

Free-flow boundary conditions across all external surfaces except the bottom (proximal) one were set in the FE model. Vertical displacements of the bottom surface were fixed, and lateral displacements of nodes in the bottom surface were fixed as shown in Figure 5c. These boundary conditions allowed for outward growth of the humerus shaft while avoiding spurious translations as well as the rotation of the whole bone rudiment.

The loading conditions applied, summarized in Figure 5d, modelled a 1-second flexion-extension cycle of the elbow. The growth resulting from a single cycle was extrapolated for multiple cycles. Loading was applied as a pressure over a roughly circular surface representing the contact areas between the radius/ulna and the humerus. A sine-like loading profile over this area was considered, with the loading area sweeping over the humerus surface. The sweep path was estimated based on anatomical observations of the axolotl elbow joint. The value of the load profile changed throughout the cycle to mimic the effect of muscle contractions, reaching the maximum value for the peak flexion position. Load step increments of 0.01s were applied. Appendix C.1 provides further details of all model parameters. We studied the effect of varying loading and boundary conditions on our computational results. In this way, we ensured the robustness of our computational setup to produce results from which to extract meaningful insights.

The material properties used, given in Appendix C.1, were either estimated from literature or based on an educated guess, except for the initial intrinsic permeability of the biphasic material. Preliminary simulations identified this parameter as having a noticeable impact on the predicted patterns. Hence, we adjusted its value based on experimental stress-relaxation data obtained through nanoindentation tests on an axolotl forelimb (Figure C.2).

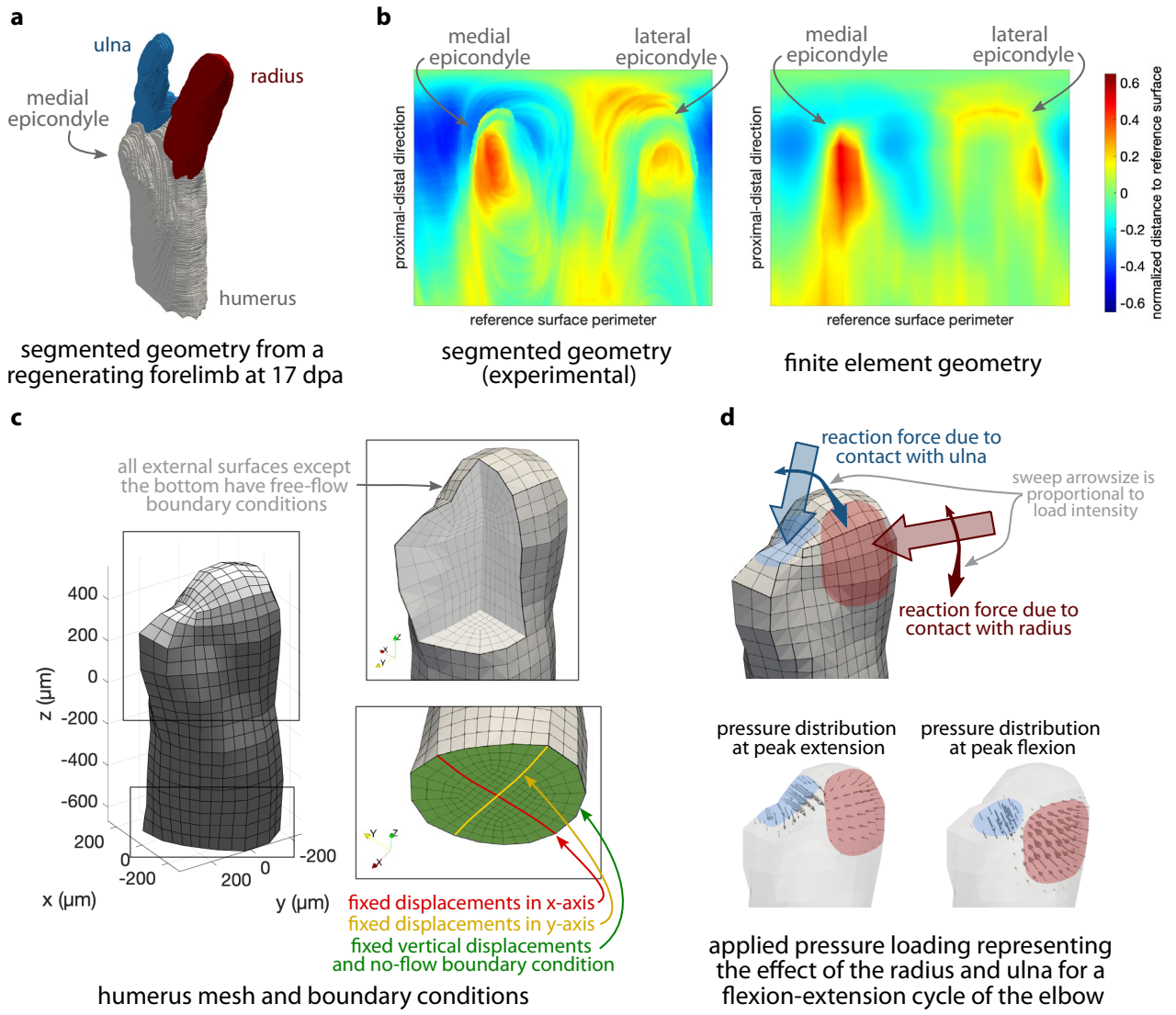

Figure 5: Finite element model of the humerus. (a) Segmentation of a regenerating forelimb at 17 dpa used as basis for the geometry. (b) 2D surface maps of the segmented humerus geometry and corresponding finite element approximation. (c) Meshed humerus and boundary conditions applied in the computational simulations. (d) Loading to simulate a flexion-extension cycle of the elbow was applied as a sweeping motion together with a twofold increase in pressure load intensity at peak flexion.

3.6 Computational predictions

The simulated flexion-extension cycle resulted in the fluid pore pressure pattern within the humerus bone rudiment shown in Figure 6a. The predicted patterns for other potential mechanical stimuli are provided in Appendix C.2. Figure 6a shows that regions of high pressure occur underneath the load representing the radius contact area throughout the cycle. However, we did not observe an analogous pressure below the load representing the ulna contact area. Pressure build up was most pronounced at the posterior proximal part of the humerus shaft. Local tissue growth due to the mechanical contribution at the end of a loading cycle is shown in Figure 6b. As expected, growth patterns matched the predicted pressure distributions. The final grown humerus for a healthy case in which both the biological and mechanical contributions were considered (Figure 6c, left) was visibly different in shape to the case in which only biological growth was taken into account, representing the mechanosensitively-impaired growth case (Figure 6c, right). For the former, local tissue growth was a combination of the results shown in Figure 6b plus a constant volumetric biological growth throughout the tissue. The latter grown shape exclusively resulted from the constant volumetric biological growth.

To quantify the differences between the two cases, we computed at each surface node the magnitude of the distance between the original surface and the grown surface, and normalized this measure with the maximum value of the two cases. We then mapped the resulting patterns onto a reference surface, fitted to the original surface mesh, and flattened it to obtain a 2D representation of normalized growth (Figure 6d). The mapping procedure followed was analogous to the one used to obtain the 2D surface maps of the experimental humeri, described in Figure 2f. For both cases, humerus surface growth increased towards the distal portion of the bone rudiment, but the the healthy growth case resulted in larger values as well as a notably asymmetrical pattern. A larger surface growth was predicted in the area corresponding to the future lateral epicondyle for the healthy growth case (Figure 6d, left).

4 Discussion

Through a combined experimental and computational approach, we have studied how limb motion during vertebrate joint formation may regulate final joint morphology. We quantified 3D humerus shape in regenerating axolotl forelimb experiments under healthy joint formation conditions (control group) and for animals with impaired mechanosensitivity in which the TRPV4 channel was targeted (GSK101 group). In parallel, we developed a biphasic poroelastic finite element model of humerus tissue growth informed by experimental data. We hypothesized growth was driven both by biological factors and by a mechanical stimuli linked to the local dynamic loading conditions in the bone rudiment. We used the computational model to explore potential physical stimuli that could be contributing to the shaping of the joint.

4.1 Impaired mechanosensitivity during joint morphogenesis altered final humerus shape

Our systematic analysis of the regenerating axolotl limbs revealed an altered humerus morphology for the mechanosensitively-impaired (GSK101) group (Figure 3a). The mean 2D surface maps computed for each group (Figure 3d) illustrate the main findings: the mean control map exhibits a darker shade of red within the epicondyles (signifying larger normalized volumes) and the shapes of the medial epicondyles are similar in the two maps; however, the lateral epicondyles are noticeably different in shape, with a much smaller red area in the GSK101 mean map. We also analyzed the normalized areas and volumes of the anterior and posterior concavities (blue

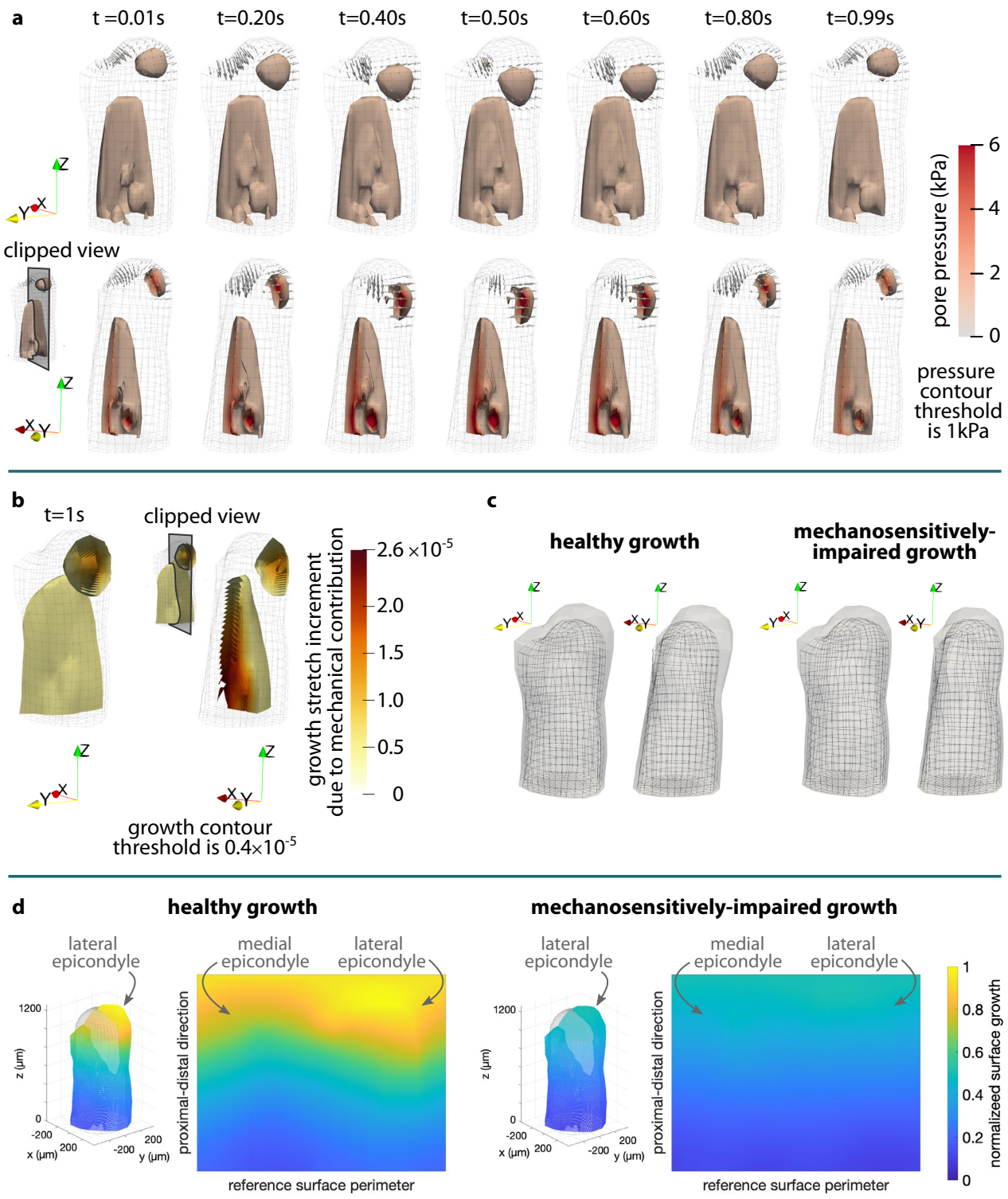

Figure 6: Computational predictions of joint morphogenesis. (a) Predicted pressure distribution in the whole humerus (top row) and in a clipped view (bottom row) over a 1-second flexion-extension cycle. (b) Local tissue growth due to the mechanical contribution at the end of one cycle. Local tissue growth due to the biological contribution was constant and not shown here. (c) Grown humerus shape representing a healthy case and a mechanosensitively-impaired case. Local tissue growth in the healthy case (left), comparable to the experimental control group, included both mechanical and biological contributions. The grown humerus shape for the mechanosensitively-impaired case (right), comparable to the experimental GSK101 group, had local tissue growth in response to the biological contribution only. In both cases growth is scaled by a factor of 3600, representing a 1-hour period, and frontal and side views are shown. (d) Quantification of grown humerus shapes based on the normalized surface growth, mapped onto a reference surface like in the experimental data analysis, and then flattened into a 2D map of normalized surface growth.

regions in the 2D surface maps of Figure A.2) following an analogous procedure to the epicondyle measurements and did not observe significant differences between groups for any measurement. Taken together, this data seems to indicate that, when unable to sense and respond to mechanical cues during joint morphogenesis, the final humerus shape is affected. Mean humerus surfaces for the control and GSK101 groups have similar shapes except for the protuberance of the epicondyles, which is more pronounced for the control case (Figure 3e). In addition, the fact that the medial epicondyle area and concavity shapes are equivalent in both groups, i.e. that these features are unaffected by mechanical stimuli, could also signify that the main shape characteristics of the humerus are already present at the onset of the joint morphogenesis stage.

Although we only analyzed a single regenerating limb after cavitation (at 17 dpa) for the purposes of developing the initial computational model, the 2D surface map obtained (Figure 5b, left) supports the notion that the basic humerus shape could be present already at this stage. We observe a clearly formed medial epicondyle in this humerus, similar in shape to those of the 33 dpa regenerated limbs in the experiments (Figure A.2). Together with the experimental findings, this implies that the medial epicondyle may form in the earlier stages of the joint formation process and its shape (as measured by the normalized area) may not be as affected by mechanical stimuli as the lateral epicondyle. The concavities also seem to already be present in the 17 dpa limb but, interestingly, the lateral epicondyle is barely discernible.

Our quantification of 3D shape in regenerating axolotl forelimbs indicates that GSK101 treatment in animals during joint morphogenesis results in altered humerus morphology. We targeted the TRPV4 ion channel with the agonist GSK101 as a means of impairing the mechanosensitive response of chondrocytes in the treated animals. Numerous studies have shown that chondrocytes have several separate but overlapping mechanotransduction pathways [27, 29]. Other channels of the TRP family have been suggested to have load-associated effects in cartilage [61], but TRPV4 is undoubtedly the major regulator of mechanical and osmotic signal transduction in this family. The PIEZO1 and PIEZO2 channels have also been identified as key stretch-induced mechanotransducers in chondrocytes [62]. It would be interesting to see whether altering these other channels has effects on morphology similar to those seen in this study, to further tease out the interrelated roles of each channel in cartilage mechanotransduction.

Alternative ways of blocking mechanics in developing joints have been used in the past to study the effect of mechanical stimuli on joint morphogenesis, namely muscle paralysis in chicks [6–10] and genetically-modified altered-muscle mice [11–13]. These studies also revealed morphological differences. Here, we used a TRPV4 agonist, which represents the clinical genetic deficits associated with abnormal skeletal development [63,64]. In addition, our 3D analysis of the humerus surface allows the assessment of shape changes that are not evident in more simple measures, such as cross-sectional outlines or linear anatomic measurements like humeral head width.

4.2 More prominent epicondyles and increased chondrocyte proliferation were not associated with larger humeri

The most striking outcome of our experimental data analysis is that the substantial reduction in cell proliferation of the GSK101 group (Figure 3a, far left, b and c) was not accompanied by smaller humeri sizes (Figure 3a, centre left). To ensure that the similar humeri fitted diameter values between the two groups were not due to an insufficiently sensitive measurement method, we computed additional metrics using an alternative methodology (see Appendix A.1). All measures of humeri shaft size computed indicted there were no significant differences between the two groups.

This apparent discrepancy could be due to the axolotl long cell cycles, which have been recorded to be up to 88 hours in regenerating tissues [65, 66]. Then, throughout the 10 day

experimental treatment, few complete cycles would have occurred. Considering that proliferating cells were only a relatively small percentage of total chondrocytes in the bone rudiment, and the small amount of cell cycles completed, maybe the total amount of cell proliferation was not enough to produce actual changes in bone rudiment size. In addition, our quantification of cell proliferation corresponded to a 18-hour window at the end of the experiment, which may not be representative of the complete treatment period.

Yet, we identified a decrease in normalized epicondyle volumes and in the lateral epicondyle area for the GSK101 group, which raises the question whether reduced cell proliferation could be related to altered humerus shape. Epicondyle cartilage growth has been linked to cell proliferation in developing chick knee joints [8]. Interestingly, regulation of chick embryo limb growth in response to motility was linked to cell proliferation only in specific growth plates in a separate study [9]. In the present study, we did not observe proliferation localized to the distal part, on the contrary it was seemingly homogeneously distributed (Figure 3b and c). Therefore, a direct link between cell proliferation location and localized tissue growth could not be made based on our experimental observations.

Chondrogenesis is driven by extracellular matrix (ECM) deposition, which is not necessarily tied to chondrocyte proliferation. Our AHA staining of the regenerated axolotl forelimbs showed no apparent difference in amount of total protein translation between the control and GSK101 animals for the 18-hour period imaged with our technique, but it is highly likely that the specific proteins that contribute to tissue growth, such as ECM proteins, could lead to increased growth in particular areas. Alternatively, directional cell growth, independent of cell proliferation, could lead to differential growth in particular areas of the tissue.

Injections in experiments started at 22 dpa as this was the estimated time of joint cavitation in the regenerating forelimbs for animals 3-5 cm in size. We subsequently analyzed a 17 dpa regenerated forelimb of a 3-cm-sized animal to develop our finite element model, which revealed that the bone rudiments were fully formed and separated, and the humerus already had a rudimentary shape, including a defined medial epicondyle. It is possible that our experiments in fact targeted the final stages of joint morphogenesis, and the bone rudiment was already close to its final size from the start of the injections. Given that regenerating limbs grow outwards from a limb bud that is created from a fully-grown stump, the proximal portion of the humerus is already correctly sized, while the joint is undergoing morphogenesis in the distal part. In contrast, during development, one would expect the joint to form as bone rudiments around it are also growing in size. Considering all the above, there are multiple possibilities as to why no difference was observed in humerus shaft size between the two experimental groups.

4.3 Local fluid pressure may promote tissue growth during joint morphogenesis

Our experimental results provide additional confirmation that mechanical forces play a role in joint morphogenesis. However, how mechanical stimuli are translated into actual tissue growth and ultimately determine joint shape is still not well understood. Our computational model of joint morphogenesis provides a complementary tool to the experimental studies. Through hypotheses and simplifying assumptions, we can isolate critical contributors to the mechanotransduction of mechanical loading into chondrogenesis and subsequent shaping of the joint.

The computational results show that compressive fluid pressure is an adequate predictor of joint morphogenesis. In the predicted normalized surface growth map for the healthy growth case (Figure 6d, left) the lateral epicondyle exhibited a considerably larger amount of growth than the medial epicondyle, which is in agreement with the larger normalized area of the lateral epicondyles and no change of the medial epicondyles identified in the experimental control group with respect to the GSK101 group (Figure 3a, far left). The predictions for the healthy growth case

also exhibited more growth towards the distal area than the mechanically-impaired one (Figure 6d, right), which only had a slight gradient in the proximo-distal direction. These differences matched our experimental findings on decreased normalized volumes in both epicondyles of the GSK101 group with respect to the control group (Figure 3a, centre left).

Certainly, our model points to a relationship between the fluid pressure distribution and the shaping of the joint. Chondrocytes might not be sensing interstitial hydrostatic pressure directly, but rather a different biophysical factor related to it. Osmotic stresses have been repeatedly identified as the stimuli triggering a series of signalling events in relation to the TRPV4 channel, that are propagated into changes in gene expression and ECM synthesis. Yet, studies have shown that osmotic loading as well as mechanical loading elicit responses of the TRPV4 channel [23,27,28,30]. Furthermore, hydrostatic and osmotic pressures have similar effects on cartilage formation [67], and they both affect intracellular ion signalling in chondrocytes [68,69]. It is not within the scope of this study to tease out the complex interrelations between the osmotic and hydrostatic pressures induced by mechanical loading on cartilage. Many studies have shown that hydrostatic pressure increases cartilage gene expression and matrix formation (see review by [70]) and, hence, we selected fluid pressure as a driver of mechanical growth in our model since it was the simplest most reasonable option. Our computational results indicate that fluid pressure can predict local tissue growth in the experimentally-informed model of joint morphogenesis developed in this study.

4.4 Poroelasticity can be used to explore how dynamic loading dictates bone rudiment morphology

Due to the nature of the poroelastic tissue, only compressive dynamic loading can generate the non-homogeneous fluid pressure pattern within the humerus that dictates tissue growth in our computational model (Figure 6a). In contrast, static loading generates an initial pressure distribution that quickly dissipates as fluid seeps out of the bone rudiment (Figure C.2c). Such behaviour is in agreement with experimental studies showing that cartilage growth is promoted by repetitive compressive loading while static loading inhibits it [37–41]. Unlike our previous models of joint morphogenesis [34, 35], we are now able to inherently capture the effect due to the type of loading imposed owing to the biphasic approach that incorporates the fluid flow component into the modelling. An earlier computational study [8] used poroelasticity to relate local patterns of biophysical stimuli to the emergence of joint shape in a model of a chick knee, but could not predict growth morphologies. Through the solid component growth, our model goes a step further and can more confidently relate local tissue growth to final bone rudiment morphology based on loading-induced mechanical stimuli.

We explored alternatives to the compressive pore pressure as mechanical stimuli for our growth model (see Appendix C.2). Several measures of compression and fluid flow in the tissue were considered, with the idea of identifying and implementing an alternative mechanical growth stimulus in our formulation. We selected the positive divergence of the seepage velocity because it is a measure of the rate of compression on the solid component of the material and its distribution within the humerus is quite different from the fluid pressure pattern (Figure C.3b, top row). The resulting local tissue growth due to the mechanical contribution was distributed more evenly towards the distal part of the humerus (Figure C.4a), instead of being localized below the radius contact loading (Figure 6b). In addition, less growth was observed in the bottom part of the humerus for the alternative model. Interestingly, this produced an apparent rotation of the humerus grown surface (Figure C.4b) rather than the slight bending and outward growth observed broadly around the lateral epicondyle region for the pressure-based mechanical growth (Figure C.1). Further study would be required to ensure artefacts due to inadequate loading or boundary conditions are not at play here before discarding the rate of tissue compression as a potential biophysical stimuli within the joint morphogenesis process.

These exploratory simulations demonstrate the potential of the proposed model as a tool to unravel the mechanisms at play in the shaping of the joint. Through the computational study of how different measures of pressure, compression, and fluid flow evolve in response to loading setups representative of in vivo conditions, we could identify potential biophysical stimuli for further study in experiments.

4.5 Future research directions

To advance in our understanding of how movement-induced loading drives joint formation, we must continue to tease out the mechanosignalling pathways in chondrocytes. Significant progress is being made in determining the activation mechanisms of TRPV4 and PIEZO ion channels. Yet, the connection across scales – from organ-level loading to molecular response – is often overlooked. How are mechanical stimuli transduced within the tissue to the cells? What biophysical measures are cells exactly responding to? Is it hydrostatic pressure, osmotic pressure, fluid velocity, strains, shear, a combination of these, or something else? New insights into cartilage mechanotransduction would have broad implications beyond the study of joint formation.

Focusing specifically on elucidating the mechanisms of joint morphogenesis, we require additional experimental studies that target other mechanosensitive channels such as PIEZO1 and PIEZO2. In this way, we could better distinguish the different mechanical stimuli involved in the shaping of the joint. Together with improved computational models, e.g. incorporating osmotic pressure into the formulation and modelling the complete joint, it would allow us to unequivocally identify the biophysical drivers of growth during joint formation.

We must expand our focus beyond the joint morphogenesis stage and continue to investigate the mechanobiology of the whole joint formation process. Our experimental findings seem to indicate that the joint already has its initial shape shortly after cavitation and mechanical loading alters this shape at the local level. It would be interesting to determine whether cavitation is influenced by mechanical stimuli or purely biologically-driven. Also of interest is the ossification process in the later stages of joint development. Further studies are required to clarify the mechanisms at play during cavitation and ossification. Emerging experimental techniques like whole mount staining and imaging provide the opportunity to explore the 3D spatial distribution of mechanosensitive growth regulators involved in cavitation (e.g. Gdf5, Noggin and Wnt) and ossification (e.g. Ihh and Pthrp) during joint formation. Developing such experiments in close association with computational modelling will provide a powerful tool that will help us advance in our understanding of the mechanobiology of joint formation.

5 Conclusions

The effect of loading-induced mechanical stimuli on joint morphogenesis was studied through the systematic quantification of 3D humeri shapes in axolotl forelimbs. Normally-regenerating limbs were compared to those of animals in which chondrocyte mechanosensitivity was impaired by the administration of a TRPV4 agonist. Results demonstrated that mechanics has a role in the shaping of the joint, but a rudimentary humerus shape seemed to be already present in the initial stage of joint morphogenesis.

We developed a finite element model of joint morphogenesis with cartilage modeled as a poroelastic material, in which growth of the solid part was due to a constant biological component as well as a loading-dependent mechanical component that includes its dynamic effects. Computational results indicated fluid pore pressure is a reasonable predictor of local tissue growth and ultimate joint shape, even if chondrocytes might not be directly sensing and responding to

hydrostatic pressure. The computational model presented provides a tool to explore alternative mechanical stimuli that may also be critical in joint morphogenesis.

Integrating experiments and computational modelling provides interesting insights that experiments alone cannot deliver. The combined approach presented in this work allowed us to validate the mechanical regulatory hypotheses with an in silico model. Such methodology will become indispensable as we advance in the study of mechanobiological processes like those involved in joint formation.

Data Accessibility The original microscopy data, the scripts used to process the data, and the computational code will be made available when the article is published.

Competing interests All authors declare they have no competing interests.

Author Contributions SJS and JRM conceived, designed and coordinated the study. JEF performed the main axolotl experiments and TJD provided additional experimental data. EC, GK, KL and TM processed the experimental data under the guidance of SJS. EC, SJS, JRM and TJD analyzed and interpreted the experimental results. EC developed the theoretical model formulation with the collaboration of SJS and JJM. EC implemented the computational model and performed the numerical simulations. EC, SJS and JJM analyzed and interpreted the computational results. EC and SJS drafted the manuscript. All authors revised and approved it for publication.

Acknowledgements The authors would like to acknowledge Eun Kyung Jeon for providing the far red nuclear stained limb image, Vineel Kondiboyina for the nanoindentation test data, Yash Kulkarni for contributing to the bone rudiment segmentations, and Soha Ben Tahar for exploratory finite element studies. EC thanks Markéta Tesařová for sharing their stl files of a newt limb.

Microscopy images were obtained from the Harvard University Center for Biological Imaging and the Northeastern University Chemical Imaging of Living Systems core. This work was completed using the Discovery cluster, supported by Northeastern University's Research Computing team. We acknowledge animal support from the Ambystoma Genetic Stock Center funded by NIH grant P40-OD019794.

Funding Statement This project has received funding from the European Union's Horizon 2020 research and innovation programme under the Marie Skłodowska-Curie grant agreement No 841047 and the National Science Foundation under grant number 1727518. JJM has been also funded by the Spanish Ministry of Science and Innovation under grant DPI2016-74929-R, and by the local government Generalitat de Catalunya under grant 2017 SGR 1278. KL was supported by a Northeastern University Undergraduate Research and Fellowships PEAK Experiences Award.

Ethics Ethics Animal experimentation: axolotls (*Ambystoma mexicanum*: d/d RRID Catalog #101L) were either bred in captivity at Northeastern University or purchased from the Ambystoma Genetic Stock Center at the University of Kentucky. Experiments were performed in accordance with Northeastern University Institutional Animal Care and Use Committee. For all experiments, animals were anaesthetised by treatment of 0.01% benzocaine until visually immobilized.

Appendix A Additional experimental results

A.1 Alternative measures of humeri shaft

Our statistical analysis of the diameters of the cylinders fitted to the humeri shaft produced no significant difference between the control and GSK101-treated groups (Figure 3a). To ensure this surprising result was not due to an insufficiently sensitive method of measurement of the humeri shaft size, we computed additional metrics using an alternative methodology.

First, we extracted a standardized portion of the humerus shaft by trimming the distal and proximal parts of the aligned humerus surface obtained in Figure 2f (left). We removed the surface portion above a vertical distance equal to the fitted diameter (measured from the most distal part along the vertical axis), and then kept a portion of the shaft equal to 0.25 times the fitted diameter in thickness. To measure the size of the extracted shaft, it was divided into 20-µm-thick slices and the surface of each slice was projected onto the cross-sectional x-y plane. The resulting 2D projected shape was converted to a binary image. Given that the extracted shafts were about 120 µm in thickness, we obtained between 5 and 7 projected 2D shapes per humerus. Finally, we computed a series of shape metrics for each projected shape and averaged the values of each for all shapes in a limb. The metrics computed were area, perimeter, equivalent diameter (i.e. the diameter of a circle with the same area as the projected shape), major axis, and minor axis.

We grouped all humeri measurements for each metric and tested for normality with a Shapiro-Wilk test. All data was normally distributed. We then used a one-way ANOVA test to compute the p-values, which were all above 0.1. Results confirm that there is no significant difference in humeri size between the control and GSK101-treated groups (Figure A.1).

A.2 Humeri 2D surface maps

The 2D surface maps of all humeri, computed following the methodology described in Section 2.2, are shown in Figure A.2. Maps have varying heights due to length variability in the segmented humerus bone rudiments. All maps have been aligned in the horizontal direction based on the centroid position of the medial epicondyle. Two control limbs had to be discarded because the segmented humerus was too short to be properly aligned following the methodology developed.

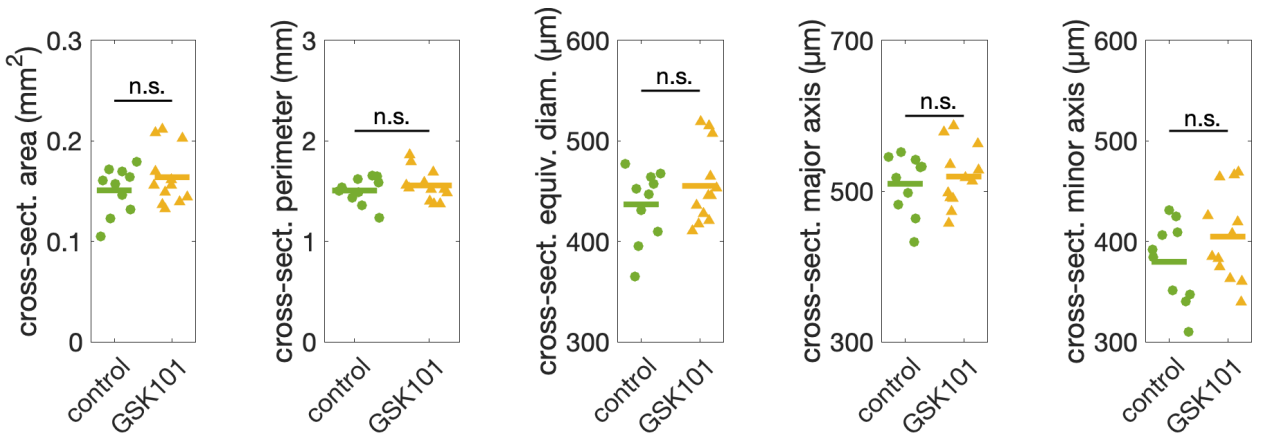

Figure A.1: Results of the statistical analysis on the data points obtained following an alternative methodology to measure humeri shaft size. All data was normally distributed (Shapiro-Wilk test) and we performed a one-way ANOVA test to obtain p-values, which were all above 0.1.

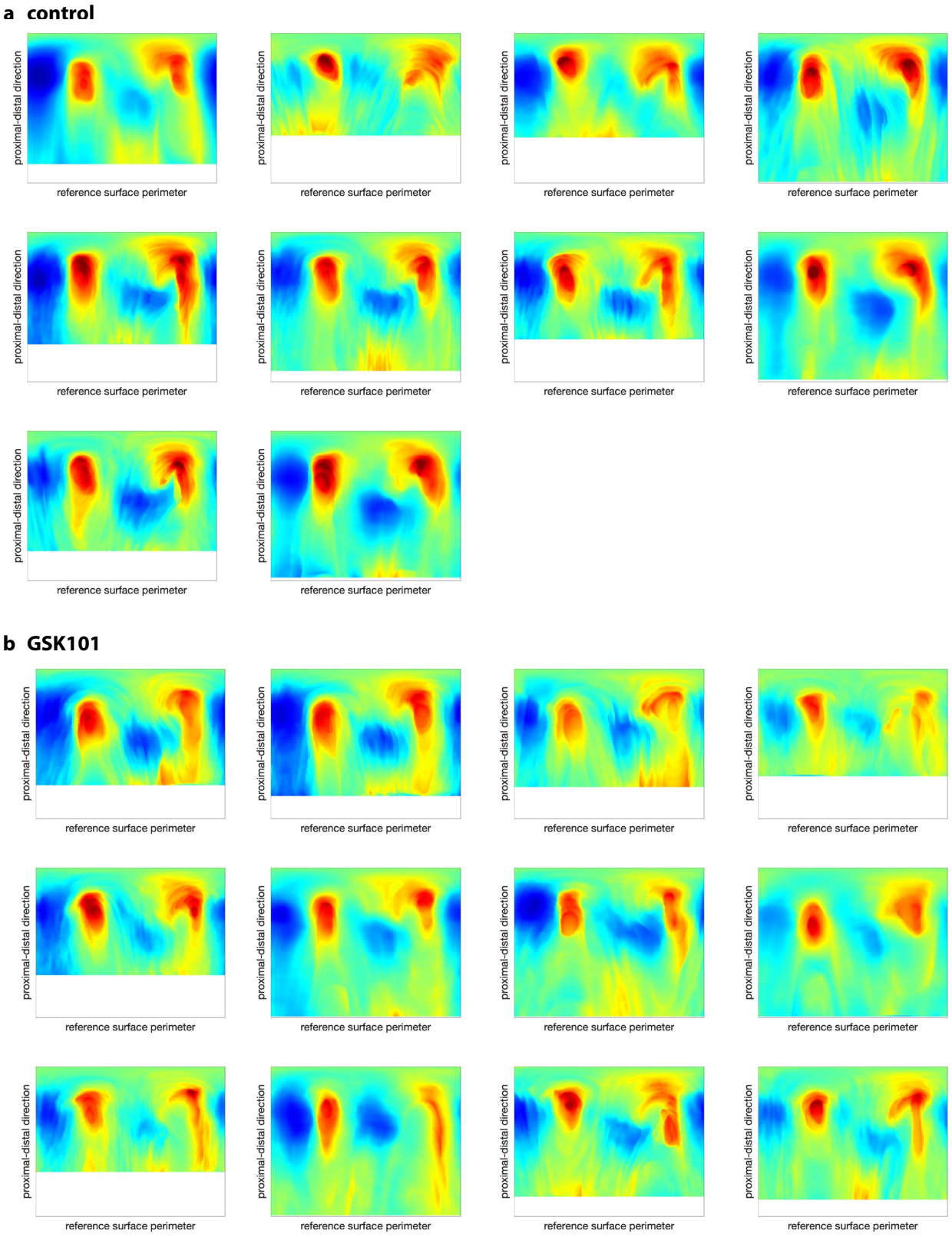

Figure A.2: Computed 2D surface maps of the humeri for (a) the control and (b) the GSK101-treated limbs.

Appendix B Numerical framework for poroelasticity with continuum growth

B.1 Introduction

We propose a finite element biomechanical model of growth at tissue level to study how specific changes in limb motion regulate joint morphology. Bone rudiments undergoing the joint morphogenesis stage are mostly composed of chondrocytes. Hence, the cartilaginous tissue is modeled as a biphasic poroelastic material consisting in a fluid-saturated nonlinear porous solid. The existing nonlinear poroelastic formulation [60] implemented in `deal.II` [59] was extended to incorporate continuum growth [71].

Here, we provide a brief overview of the poroelastic formulation and describe the derivation and implementation of the continuum growth portion of the computational model.

B.2 Kinematics

The biphasic material is composed of a hyperelastic solid skeleton (S) and a pore fluid constituent (F) that occupy simultaneously a given spatial position $\boldsymbol{x}$ in the current configuration at time t. Then, the constituent deformation map is $\boldsymbol{x} = \chi_S(\boldsymbol{X}_S, t) = \chi_F(\boldsymbol{X}_F, t)$, where $\boldsymbol{X}_S$ and $\boldsymbol{X}_F$ correspond to the different material positions in the reference configuration at the reference time t_0 of the solid and fluid constituents, respectively. The solid displacement is $\boldsymbol{u}_S = \boldsymbol{x} - \boldsymbol{X}_S$, and its material deformation gradient is $\boldsymbol{F}_S = \partial \boldsymbol{x}/\partial \boldsymbol{X}_S$, where the subscript '$S$' will be dropped for clarity in the subsequent derivations. The seepage velocity describes the motion of the fluid with respect to the deforming solid material, i.e. $\boldsymbol{w}_F = \boldsymbol{v}_F - \boldsymbol{v}_S = \partial \chi_S/\partial t - \partial \chi_F/\partial t$.

Note that the solid and fluid constituents are assumed to be separately incompressible, but the biphasic material is compressible owing to the fluid flow within the pores of the deforming solid skeleton. In addition, the saturation condition establishes $n^S + n^F = 1$, where n^S and n^F are the volume fractions of the solid and fluid constituents, respectively. Based on the volume balance of the solid skeleton, the former can be integrated towards $n^S = n^S_{0S}/J$, where $J = \det(\boldsymbol{F}) > 0$ and n^S_{0S} is the initial solid volume fraction, a measure of the biphasic material's initial porosity.

B.3 Continuum growth

We introduce volumetric tissue growth through the multiplicative decomposition of the material deformation gradient tensor of the solid component,

$$\boldsymbol{F} = \boldsymbol{F}^e \cdot \boldsymbol{F}^g \quad \text{with} \quad \boldsymbol{F}^g = \vartheta \mathbf{1}. \tag{1}$$

The rate of the growth stretch ϑ determines the isotropic growth, and $J^e = \det(\boldsymbol{F}^e) > 0$ is the Jacobian of the elastic part of the material deformation gradient tensor of the solid component, $\boldsymbol{F}^e$.

Following past studies [33, 34], we hypothesize that growth stretch rate is given by the sum of a biological and a mechanical contributions,

$$\dot{\vartheta} = \dot{\vartheta}_b + \dot{\vartheta}_m. \tag{2}$$

The rationale is that certain growth will occur during limb formation regardless of external mechanical stimuli, owing to morphogenetic cues that result, for example, in cell proliferation and extracellular matrix deposition. The amount of biological growth is, therefore, assumed to be proportional to chondrocyte density, C_d. We experimentally measured chondrocyte density in a regenerated axolotl humerus and found that it was approximately constant along its proximo-distal

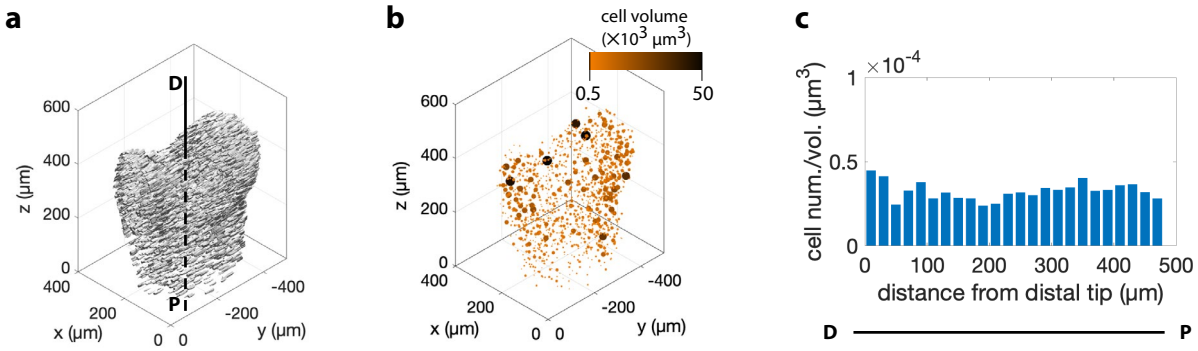

Figure B.1: Experimental data used to determine a constant biological growth function. (a) The chondrocyte nuclei outlines were extracted from a far red nuclear staining 3D light sheet image stack of a regenerated axolotl forelimb using Cellpose [72]. Cell nuclei surfaces are shown in 3D space after vertically aligning the proximo-distal (P-D) axis of the humerus in Matlab [52]. (b) Cell nuclei positions and corresponding volumes in 3D space were obtained with the Fiji plugin 3D Objects Counter [49], imported and aligned in Matlab. Outliers were removed based on the cut-off volumes 0.5×10^3 and 50×10^3 µm. (c) Cell density was computed as cell number divided by cross-sectional slice volume, and plotted along the proximo-distal axis. A thickness of 20 µm was used to compute the humeri cross-sectional slice volumes from a segmentation of the whole humerus bone rudiment based on the original 3D image stack.

axis (see Figure B.1). For this reason, we used a constant biological growth function,

$$\dot{\vartheta}_b\left(C_d\right) = k_b, \tag{3}$$

where the parameter k_b modulates the rate of tissue growth due to intrinsic biological factors. The mechanical contribution is proportional to the biophysical stimuli Ξ, hypothesized to drive local tissue growth. For simplicity, we started our numerical explorations assuming the positive (compression) pore pressure was driving the mechanical portion of tissue growth,

$$\dot{\vartheta}_m\left(\Xi\right) = k_m\,\Xi = k_m < p >, \tag{4}$$

where the parameter k_m adjusts the proportion of mechanical growth to the overall tissue growth, and the Macauley brackets $< \bullet >$ indicate that only positive (compressive) fluid pressure produces mechanical growth. We note that in addition to $\Xi =< p >$, and in order to explore different feedback mechanisms, other alternative mechanical stimuli have been tested, such as $\Xi =< \mathrm{div}\left(\boldsymbol{w}\right) >$, which is a measure of local solid component compression rate.

The algorithm used to implement continuum growth in the poroelastic model is given in Figure B.2.

B.4 Governing field equations

Following standard assumptions as described in [60], the governing field equations are derived from the mass continuity and local linear momentum balance equations of the individual material components. The resulting weak form of the overall linear momentum balance is

$$\int_{\mathcal{B}_0} \nabla(\delta\boldsymbol{u}) : \boldsymbol{\tau}\,\mathrm{d}V_{0S} - \int_{\partial\mathcal{B}_0^T} \delta\boldsymbol{u}\cdot\boldsymbol{T}^*\,\mathrm{d}A_{0S} = 0 \qquad \forall\delta\boldsymbol{u}, \tag{5}$$

and the overall mass balance is

$$\int_{\mathcal{B}_0} \delta p\,\dot{J}_e\,\mathrm{d}V_{0S} - \int_{\mathcal{B}_0} \nabla(\delta p)\cdot\boldsymbol{w}J\,\mathrm{d}V_{0S} = 0. \qquad \forall\delta p. \tag{6}$$

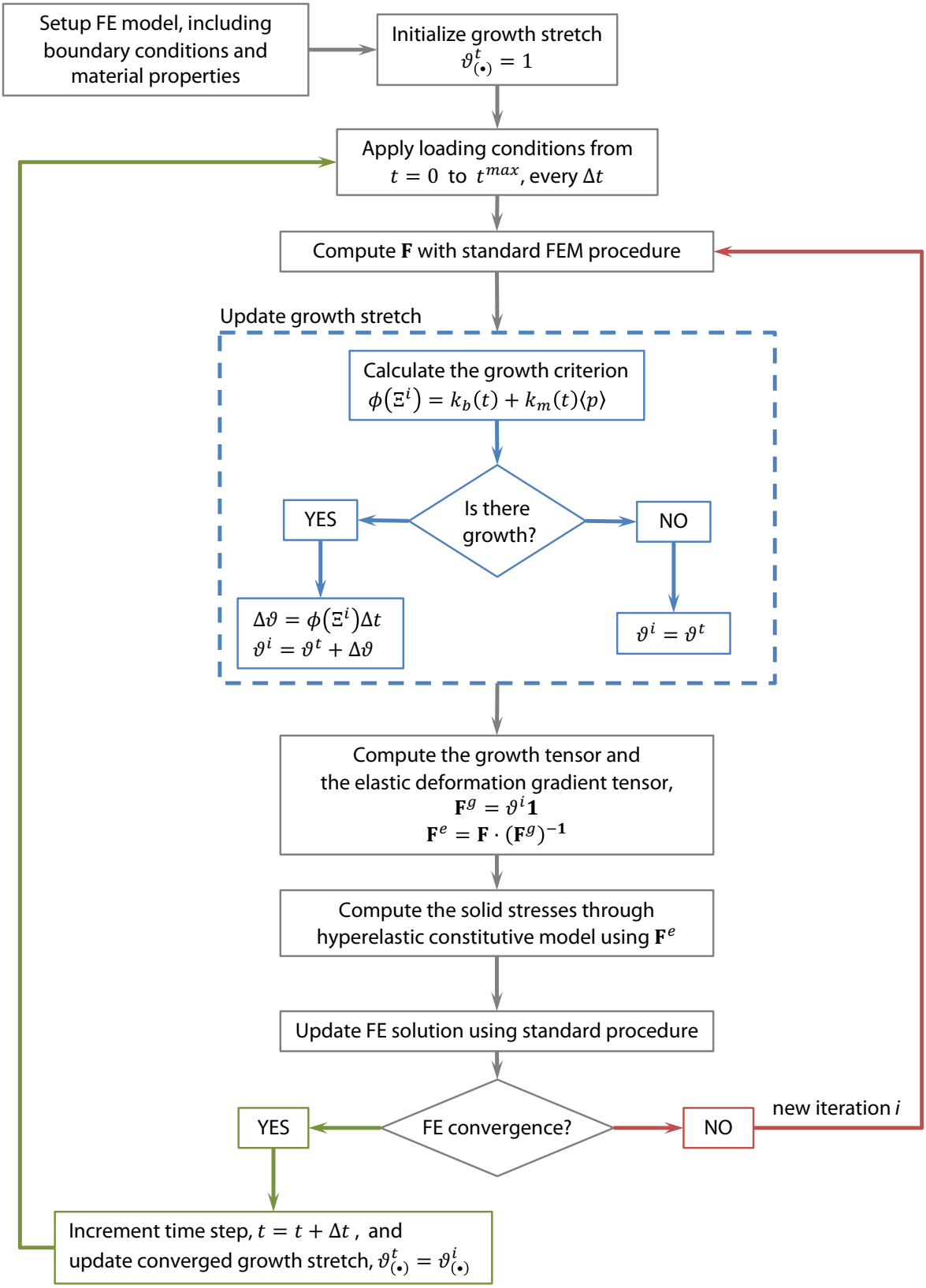

Figure B.2: Algorithm for the numerical implementation of growth in the poroelastic finite element formulation used. Adapted from [71], the growth stretch in this study does not have a limiting function. The growth increment $\Delta\vartheta$ can be computed directly because the growth criterion is independent of previous values of ϑ^t. The growth rate parameters k_b and k_m are time-step dependent to ensure no growth is applied in the first and last time steps, corresponding to the application and removal of the loading conditions.

Both equations are given in the reference configuration and introduce the solid displacement test function δu and the fluid pore pressure test function δp, respectively. The Kirchhoff stress tensor $\boldsymbol{\tau}$ in (5) is defined by the constitutive equation of the solid component (see next Section) and $\boldsymbol{T}^*$ is the prescribed traction on the boundary $\mathcal{B}_0^T$. Here, we have neglected volumetric forces due to the effect of gravity. The volume-weighted seepage velocity $\boldsymbol{w} = n^F \boldsymbol{w}_F$ introduced in (6) is defined by the constitutive equation of the fluid. The term $\dot{J}_e$ indicates the material time derivative of the Jacobian of the elastic deformation gradient tensor. Here, we do not prescribe forced fluid flow across the boundaries.

B.5 Constitutive models

The hyperelastic solid behaviour is given by the constitutive equation

$$\boldsymbol{\tau} = \boldsymbol{\tau}_E^{\mathrm{NH}} + \boldsymbol{\tau}_E^{\mathrm{vol}} - p\, J\, \mathbf{1}, \tag{7}$$

where the 'extra' stress is split into a neo-Hookean contribution,

$$\boldsymbol{\tau}_E^{\mathrm{NH}} = \mu \left[\boldsymbol{F}_e \cdot \boldsymbol{F}_e^T - \mathbf{1} \right], \tag{8}$$

and a volumetric term, which accounts for the compressibility effects of the biphasic material,

$$\boldsymbol{\tau}_E^{\mathrm{vol}} = \lambda \left[1 - n_{0S}^S \right]^2 \left[\frac{J_e}{1 - n_{0S}^S} - \frac{J_e}{J_e - n_{0S}^S} \right] \mathbf{1}. \tag{9}$$

Here, we introduce the neo-Hookean shear modulus μ and the first Lamé parameter λ.

A Darcy-like law is used to define the fluid constitutive behaviour,

$$\boldsymbol{w} = -\frac{1}{\mu^{\mathrm{FR}}} \left[\frac{J - n_{0S}^S}{1 - n_{0S}^S} \right] \boldsymbol{K}_0^S \cdot \nabla p, \tag{10}$$

where, for simplicity, gravity contributions have been neglected. Here we introduce the effective shear viscosity of the fluid, μ^{FR} and the initial intrinsic permeability $\boldsymbol{K}_0^S = K_0 \mathbf{1}$, which is assumed to be isotropic.

Appendix C Details of the computational model and additional results

C.1 Model parameters

The material parameters used in the computational simulations are summarized in Table C.1. In the definition of the solid component behaviour, we selected the neo-Hookean shear modulus and the initial solid volume fraction based on values found in literature [54, 73]. The first Lamé parameter was set to a value roughly two orders of magnitude higher than the shear modulus to ensure correct enforcement of the compaction point behaviour and of the incompressibility of the solid component. Given the small loading values applied in our simulations, predicted deformations throughout our model were always far from this point and, hence, this value does not impact the predicted patterns. The fluid component behaviour was defined through the initial intrinsic permeability and the fluid viscosity. Preliminary simulations revealed that the value of the former had a considerable impact on the predicted pressure patterns. Therefore, initial intrinsic permeability was estimated based on experimental data, as explained below. The fluid viscosity

was set to that of water at 25°C. Finally, the parameters regulating the contribution of the mechanical and biological growth rates to the overall tissue growth were manually adjusted to obtain a reasonable proportion between the two contributions for the healthy case.

A loading pressure range between 10 kPa at peak extension and 20 kPa at peak flexion was applied. This value is a rough guess based on the maximum muscle stress reported for tiger salamanders [74] (obtained for an animal mass of 1.3 g, which is the mean mass of the axolotls in our study) and an extrapolation of the relative cross-sections between the limb muscle and bone rudiment morphologies of a Spanish ribbed newt [75]. The increase in load intensity can be interpreted as a representation of the changes in contact force between the bone rudiments due to muscle contractions driving the limb flexion-extension motion. Contact area and sweep path were estimated based on the bone rudiment 3D surfaces extracted from experimental data.

Initially, the whole external surface of the humerus was set to allow free fluid flow across it. Upon close analysis of preliminary results, we considered that a bottom surface with no-flow condition approximated better the in vivo conditions of the humerus bone rudiment. Figure C.1 shows the results obtained in our study of the effect that the flow boundary condition in the bottom surface has on predicted local tissue growth. We simulated the ulna and radius contact separately with the goal of discerning the contribution of each load to the predicted patterns. For each bone rudiment we considered only the sweeping motion without any load intensity change and, then, a fixed position but a load intensity change. Growth predictions for a free-flow and a no-flow bottom surface are roughly equivalent in the distal portion of the humerus for any given loading condition. Close to the bottom surface, differences in growth appear due to different pressure patterns predicted for the free-flow vs no-flow conditions. A free-flow bottom boundary condition enforces all nodes in the surface to have a zero pressure value, which prevents pressure build up above the surface. Ideally, we would want to avoid artefacts like these, which arise from a fictitious boundary, by modelling the complete bone rudiment. However, due to computational limitations and because we are interested in the growth of the distal portion of the humerus, we deemed that the approximation provided by our model was sufficient for the purposes of this study.

This set of simulations also served to confirm that the contribution of the radius loading to growth is much larger than that of the ulna loading. In our main simulations we combined sweeping motion with load intensity increment for both ulna and radius loading. In this way we simulated the change in contact position between bone rudiments during a flexion-extension movement (sweeping motion) as well as changes in reaction force between bone rudiments in contact owing to the effect of muscles contracting.

Time steps of 0.01s were applied for a total of 1.01s to reproduce a flexion-extension cycle. Load value increased in a sinusoidal manner, as did the sweeping motion where the load was ap-

Table C.1: Material parameters used in the computational simulations.

Parameter	Symbol	Value	Units
solid shear modulus	μ	2.0e3	kPa
first Lamé parameter	λ	1.0e5	kPa
initial solid volume fraction	n^S_{0S}	0.17	
initial intrinsic permeability	K_0	1.0e-3	µm^2
fluid viscosity	μ_{FR}	0.89	kPa·s
biological growth rate parameter	k_b	2.0e-5	s^{-1}
mechanical growth rate parameter	k_m	1.0e-5	(kPa·s)$^{-1}$

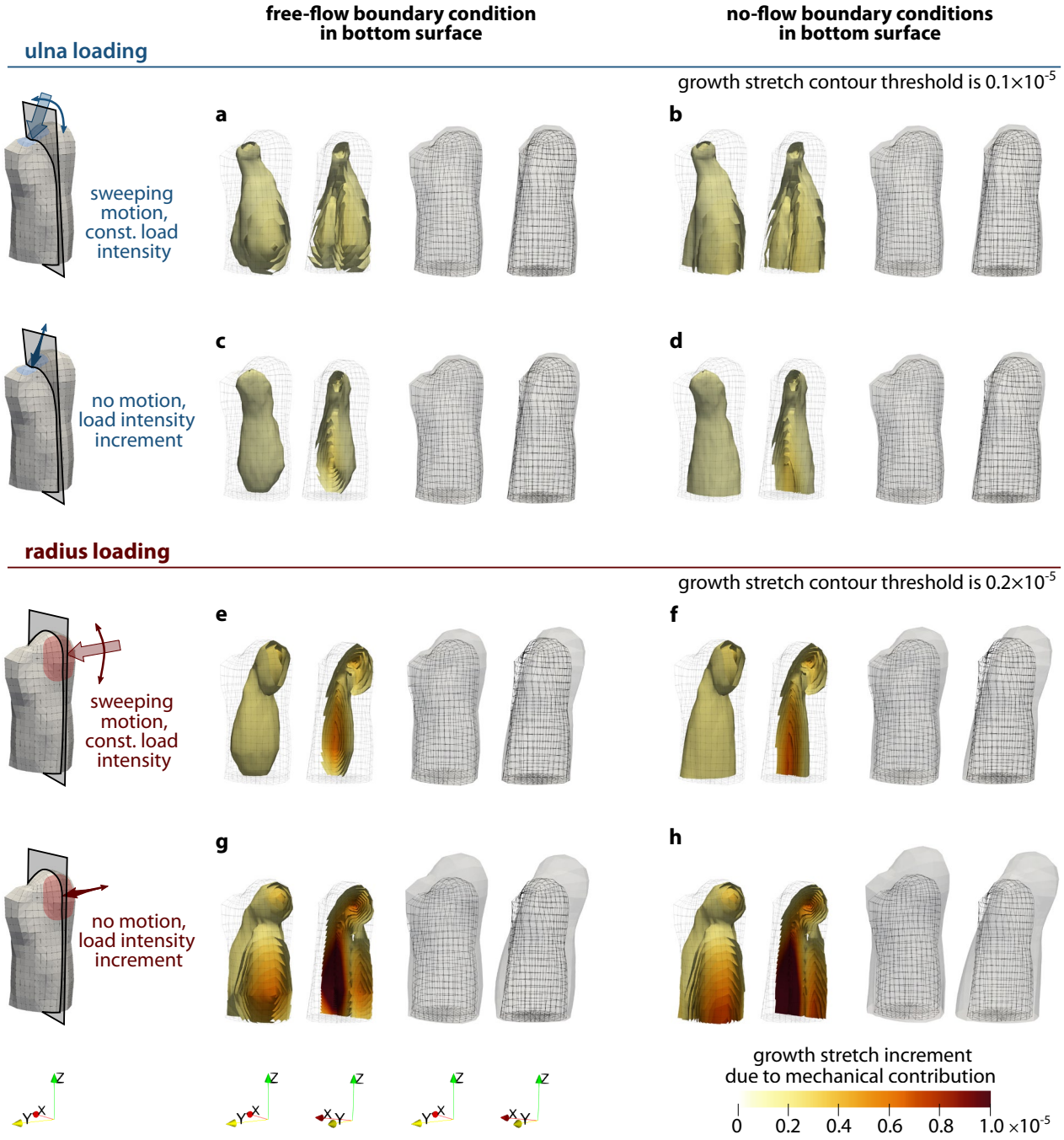

Figure C.1: Computational predictions for free-flow and no-flow boundary conditions in the bottom surface. Results are shown separately for ulna and radius loading, with sweeping motion and load intensity change also studied separately. For each loading and boundary conditions combination the left-most image shows the growth stretch increment distribution in the humerus and the centre left image shows a clipped view of the same result. Growth shown is exclusively due to the mechanical contribution, with $k_m = 5 \cdot 10^{-4}$ (kPa·s)$^{-1}$ at the end of a flexion-extension load cycle. The centre right and right-most images of each simulation correspond to the frontal and side views of the grown humerus shape. For all cases, growth computed after a 1-second-cycle is scaled by a factor of 36000, representing 10 hours of loading.

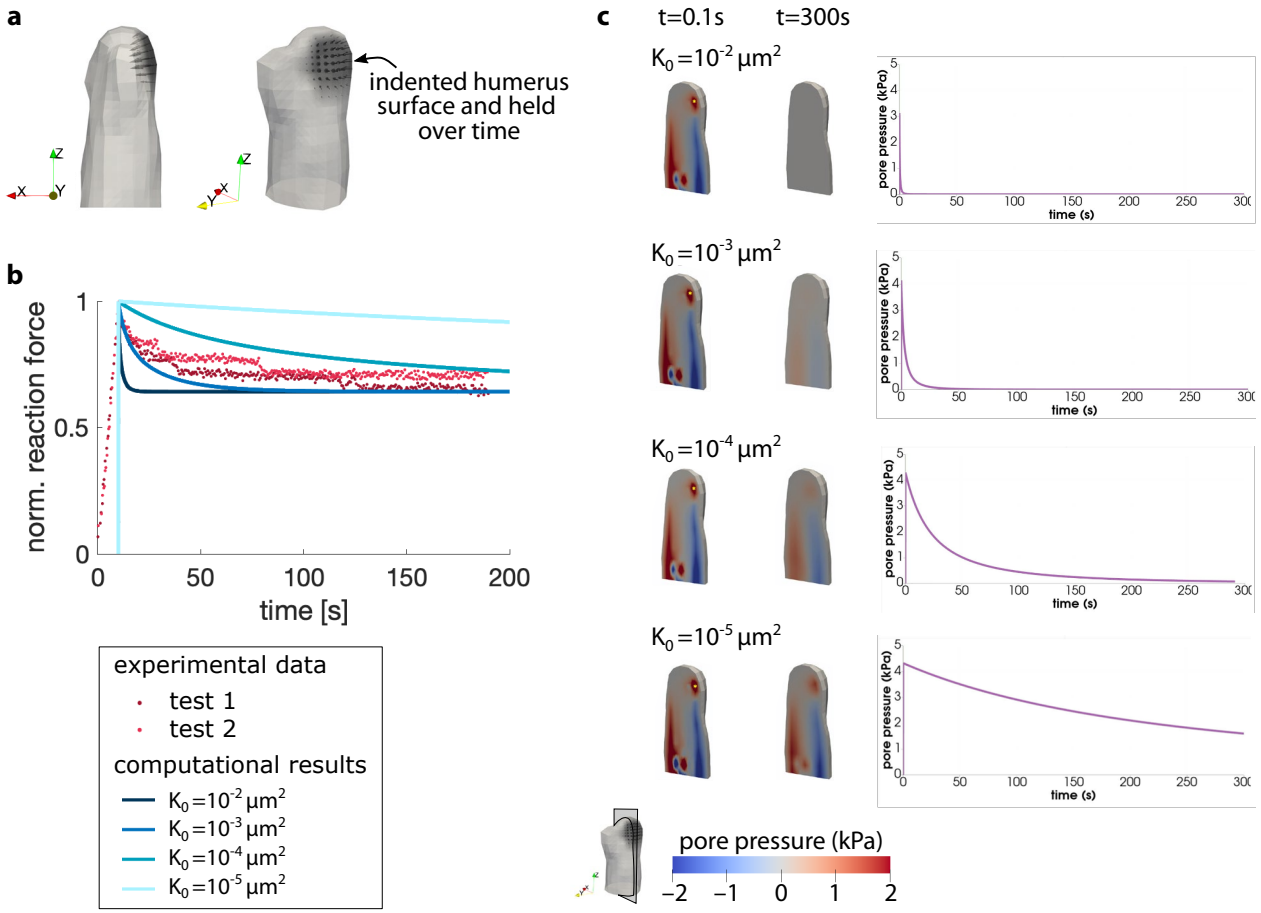

Figure C.2: Adjustment of the initial intrinsic permeability based on experimental data. (a) Stress-relaxation computational model used. (b) Reaction force obtained in the nanoindentation experiments on an axolotl limb bone rudiment (dots) and reaction force computed in the stress-relaxation model for different values of K_0 (lines). Reaction force is normalized with its peak value over time for each example. (c) Pressure distribution at the initial (left column) and final (middle column) time steps in a a vertical cross-section of the humerus (shown bottom left) for the different values of K_0. The evolution of the pressure value at the point marked with a yellow asterisk in the left column is shown over time in the right column.

plied. The use of sinusoidal increments avoids abrupt changes in the numerical simulation, which are known to produce unrealistic peaks in predicted variable values. In fact, this is why growth was not applied in the first and last step, when the load was applied and removed. Preliminary simulations were run to ensure time step size was not affecting the predicted outcomes. We observed comparable pressure patterns for simulations with same material parameters, boundary conditions and loading patterns.

Figure C.2 shows the stress-relaxation model we used to identify the initial intrinsic permeability value, $K_0 = 10^{-2}$ µm. We compared computational predictions to experimental data from a nanoindentation test on an axolotl bone rudiment. The indentation rate was 100 nm/s and the maximum indentation distance of 5 µm was applied with an indenter of radius 25 µm. Relaxation was recorded over a 3-minute period. We predicted a similar stress-relaxation condition in our material by applying a static load on the distal part of the humerus (Figure C.2a). We then measured the total reaction force of the loaded surface over time for different values of K_{0s} and compared them to the experimental results (Figure C.2b). This computational example illustrates the advantage of using a poroelastic material model instead of an elastic one. We are able to explicitly capture the relaxation of the material under a static load. In this way, we can predict (and adjust) the dissipation of the pressure accumulated below the loading surface as fluid seeps out of the sample and the material returns to its relaxed state (Figure C.2c).

C.2 Exploring alternative mechanical stimuli for growth

We hypothesized pore pressure is the mechanical stimuli driving local tissue growth. Our results show that predicted humerus grown shapes using pressure as a driver of mechanical growth are consistent with experimental findings. However, it is not clear what are the exact biophysical stimuli that chondrocytes sense and respond to. The numerical framework set up in this study provides the opportunity to easily explore alternative stimuli for growth. Figure C.3 shows the predicted distribution over a flexion-extension cycle of several variables that could potentially better represent the stimuli sensed by chondrocytes.

The volume-weighted seepage velocity $\boldsymbol{w}$ is the relative velocity of the pore fluid with respect to the deforming solid skeleton. Its L_2-norm is a measure of the amount of fluid flow (Figure C.3a), while its divergence indicates the rate of compression or expansion on the solid component for positive or negative values, respectively (Figure C.3b). We also computed the increment of a scalar norm of the solid component stretches,

$$\Delta\text{norm}(\boldsymbol{\lambda}_S) = \sqrt{\left(\lambda_x^2 + \lambda_y^2 + \lambda_z^2\right)/3} - 1, \tag{11}$$

where λ_x, λ_y and λ_z are the stretches of the solid in the global coordinates. A positive increment indicates expansion of the solid while a negative one is representative of compression (Figure C.3c).

Interestingly, the general pattern of the norm of the seepage velocity (Figure C.3a) and the negative increment of the norm of the solid stretches (Figure C.3c, middle row) resemble the predicted pressure patterns and would probably result in similar growth predictions. However, the rate of compression (Figure C.3b, top row) produces a noticeably different pattern. We also tested to modify the mechanical growth equation (4) in our model, replacing pressure with the divergence of the velocity. The predicted local tissue growth and resulting humerus grown shape are shown in Figure C.4. A value of $k_m = 10$ was used to obtain local tissue growth of the same order of magnitude as in our previous simulations. The grown humerus shape showed considerably less amount of surface growth and appeared to rotate instead of bend like in the pressure-driven mechanical growth predictions. Further studies would have to be conducted to explore the effect of loading and boundary conditions on this model. Yet, these preliminary results demonstrate the potential of the computational framework proposed here for exploring how different mechanical stimuli could be driving local tissue growth and ultimately shaping the joint.

Figure C.3 ***(following page)*****:** Alternative mechanical stimuli to consider for the finite element growth model. The computational predictions for the evolution of the following variables is shown for a flexion-extension cycle in the humerus. (a) Distribution of the L_2-norm of the seepage velocity in the humerus (top row) and in a clipped view (bottom row), both given in µm/s. (b) Distribution of the divergence of the seepage velocity, given in s^{-1}. A positive value indicates rate of solid compression (top row) while a negative one indicates rate of solid expansion (bottom row). (c) Distribution of the increment of a scalar norm of the solid stretch. A positive increment indicates solid expansion (top row) while a negative one indicates solid compression (middle row). The two are superimposed in a clipped view of the humerus (bottom row).

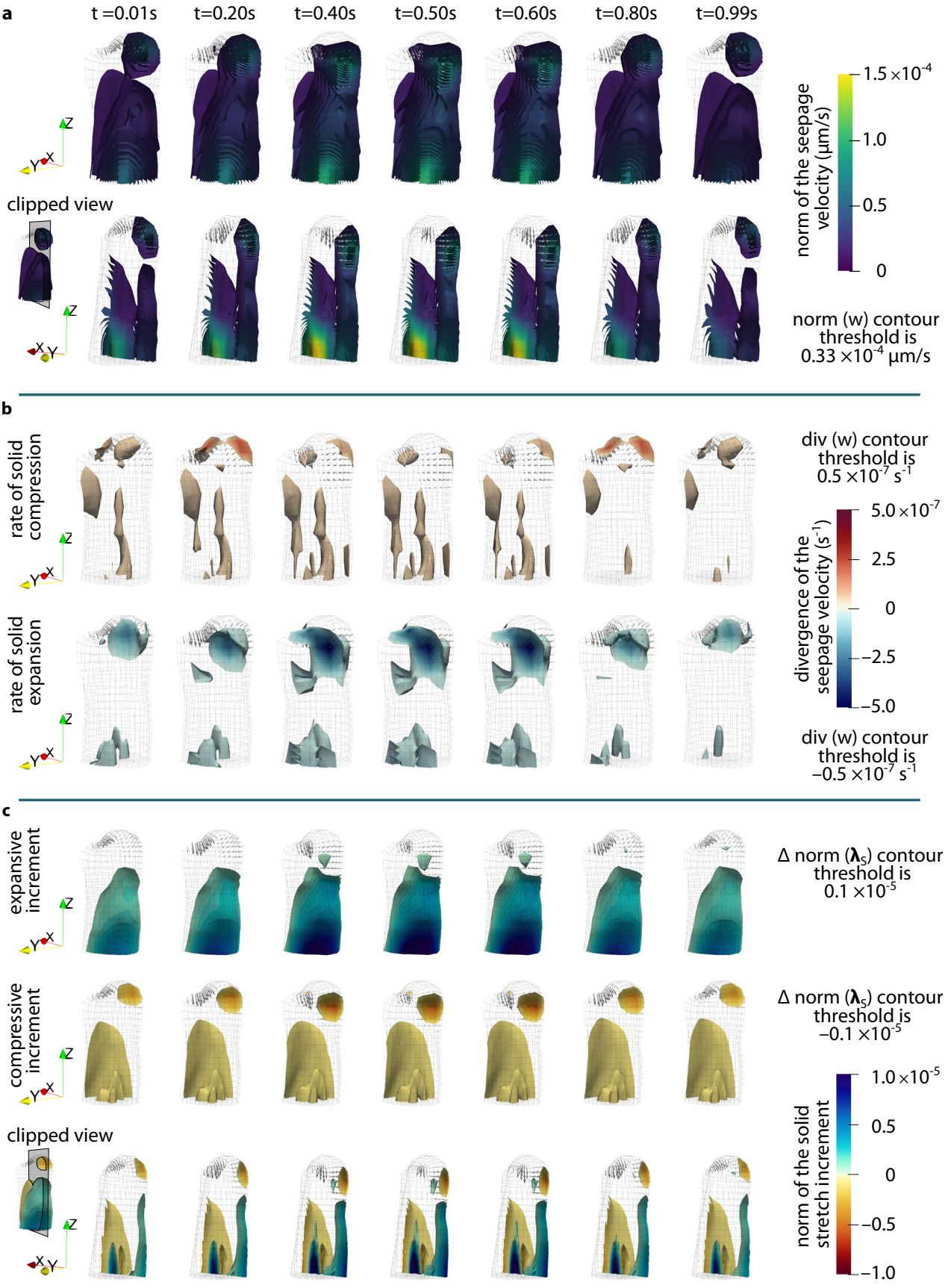

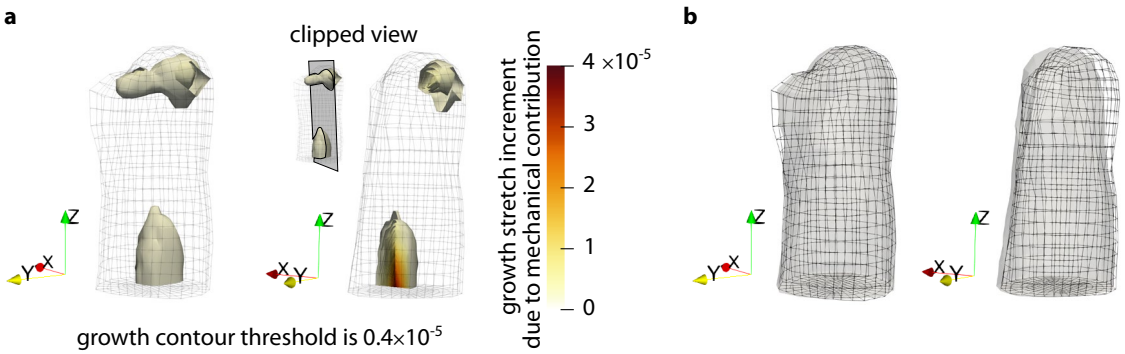

Figure C.4: Finite element growth model using $< \mathrm{div}\,(\boldsymbol{w}) >$ (positive divergence of the seepage velocity, a measure of the rate of solid compression) as mechanical stimulus. (a) Computational predictions of the local tissue growth due to the mechanical contribution at the end of one flexion-extension cycle. Distribution in the whole humerus (left) and in a clipped view (right). (b) Grown humerus shape scaled by a factor of 86400, representing 24 hours of loading. A frontal view (left) and a side view (right) are shown.

References

[1] Pacifici M, Koyama E, Iwamoto M. Mechanisms of synovial joint and articular cartilage formation: Recent advances, but many lingering mysteries. Birth Defects Res C Embryo Today. 2005;75(3):237–248. doi: 10.1002/bdrc.20050.

[2] Khan IM, Redman SN, Williams R, Dowthwaite GP, Oldfield SF, Archer CW. The Development of Synovial Joints. In: Curr Top Dev Biol. vol. 79. Academic Press; 2007. p. 1–36. doi: 10.1016/S0070-2153(06)79001-9.

[3] Nowlan NC, Sharpe J, Roddy KA, Prendergast PJ, Murphy P. Mechanobiology of embryonic skeletal development: Insights from animal models. Birth Defects Res C Embryo Today. 2010;90(3):203–213. doi: 10.1002/bdrc.20184.

[4] Nowlan NC, Sharpe J. Joint shape morphogenesis precedes cavitation of the developing hip joint. J Anat. 2014;224(4):482–489. doi: 10.1111/joa.12143.

[5] Shea CA, Rolfe RA, Murphy P. The importance of foetal movement for co-ordinated cartilage and bone development in utero: Clinical consequences and potential for therapy. Bone Joint Res. 2015;4(7):105–116. doi: 10.1302/2046-3758.47.2000387.

[6] Mikic B, Wong M, Chiquet M, Hunziker EB. Mechanical modulation of tenascin-C and collagen-XII expression during avian synovial joint formation. J Orthop Res. 2000;18(3):406–15. doi: 10.1002/jor.1100180312.

[7] Osborne AC, Lamb KJ, Lewthwaite JC, Dowthwaite GP, Pitsillides AA. Short-term rigid and flaccid paralyses diminish growth of embryonic chick limbs and abrogate joint cavity formation but differentially preserve pre-cavitated joints. J Musculoskelet Neuronal Interact. 2002;2(5).

[8] Roddy KA, Prendergast PJ, Murphy P. Mechanical influences on morphogenesis of the knee joint revealed through morphological, molecular and computational analysis of immobilised embryos. PLoS ONE. 2011;6(2):e17526. doi: 10.1371/journal.pone.0017526.

[9] Pollard AS, Charlton BG, Hutchinson JR, Gustafsson T, McGonnell IM, Timmons JA, et al. Limb proportions show developmental plasticity in response to embryo movement. Sci Rep. 2017;7. doi: 10.1038/srep41926.

[10] Bridglal DL, Boyle CJ, Rolfe RA, Nowlan NC. Quantifying the tolerance of chick hip joint development to temporary paralysis and the potential for recovery. Dev Dyn. 2021;250(3):450–464. doi: 10.1002/dvdy.236.

[11] Kahn J, Shwartz Y, Blitz E, Krief S, Sharir A, Breitel DA, et al. Muscle Contraction Is Necessary to Maintain Joint Progenitor Cell Fate. Dev Cell. 2009;16(5):734–743. doi: 10.1016/j.devcel.2009.04.013.

[12] Nowlan NC, Bourdon C, Dumas G, Tajbakhsh S, Prendergast PJ, Murphy P. Developing bones are differentially affected by compromised skeletal muscle formation. Bone. 2010;46(5):1275–1285. doi: 10.1016/j.bone.2009.11.026.

[13] Sotiriou V, Rolfe RA, Murphy P, Nowlan NC. Effects of Abnormal Muscle Forces on Prenatal Joint Morphogenesis in Mice. J Orthop Res. 2019;37(11):2287–2296. doi: 10.1002/jor.24415.

[14] Brunt LH, Skinner REH, Roddy KA, Araujo NM, Rayfield EJ, Hammond CL. Differential effects of altered patterns of movement and strain on joint cell behaviour and skeletal morphogenesis. Osteoarthritis Cartilage. 2016;24(11):1940–1950. doi: 10.1016/j.joca.2016.06.015.

[15] Guimond JC, Lévesque M, Michaud PL, Berdugo J, Finnson K, Philip A, et al. BMP-2 functions independently of SHH signaling and triggers cell condensation and apoptosis in regenerating axolotl limbs. BMC Dev Biol. 2010;10:15. doi: 10.1186/1471-213X-10-15.

[16] Fröbisch NB, Shubin NH. Salamander limb development: Integrating genes, morphology, and fossils. Dev Dyn. 2011;240(5):1087–1099. doi: 10.1002/dvdy.22629.

[17] Cosden-Decker RS, Bickett MM, Lattermann C, MacLeod JN. Structural and functional analysis of intra-articular interzone tissue in axolotl salamanders. Osteoarthritis Cartilage. 2012;20(11):1347–1356. doi: 10.1016/j.joca.2012.07.002.

[18] Lee J, Gardiner DM. Regeneration of Limb Joints in the Axolotl (Ambystoma mexicanum). PLoS ONE. 2012;7(11):e50615. doi: 10.1371/journal.pone.0050615.

[19] Wang JHC, Thampatty BP. An introductory review of cell mechanobiology. Biomech Model Mechanobiol. 2006;5(1):1–16. doi: 10.1007/s10237-005-0012-z.

[20] O'Conor CJ, Case N, Guilak F. Mechanical regulation of chondrogenesis. Stem Cell Res Ther. 2013;4(4):61. doi: 10.1186/scrt211.

[21] Gilbert SJ, Blain EJ. Cartilage mechanobiology: How chondrocytes respond to mechanical load. In: Mechanobiology in Health and Disease. Elsevier Ltd.; 2018. p. 99–126. doi: 10.1016/B978-0-12-812952-4.00004-0.

[22] Muramatsu S, Wakabayashi M, Ohno T, Amano K, Ooishi R, Sugahara T, et al. Functional gene screening system identified TRPV4 as a regulator of chondrogenic differentiation. J Biol Chem. 2007;282(44):32158–32167. doi: 10.1074/jbc.M706158200.

[23] O'Conor CJ, Leddy HA, Benefield HC, Liedtke WB, Guilak F. TRPV4-mediated mechanotransduction regulates the metabolic response of chondrocytes to dynamic loading. Proc Natl Acad Sci U S A. 2014;111(4):1316–21. doi: 10.1073/pnas.1319569111.

[24] Savadipour A, Nims RJ, Katz DB, Guilak F. Regulation of chondrocyte biosynthetic activity by dynamic hydrostatic pressure: the role of TRP channels. Connect Tissue Res. 2021;p. 1–13. doi: 10.1080/03008207.2020.1871475.

[25] Clark AL, Votta BJ, Kumar S, Liedtke W, Guilak F. Chondroprotective role of the osmotically sensitive ion channel transient receptor potential vanilloid 4: Age- and sex-dependent progression of osteoarthritis in Trpv4-deficient mice. Arthritis Rheum. 2010;62(10):2973–2983. doi: 10.1002/art.27624.

[26] Zelenski NA, Leddy HA, Sanchez-Adams J, Zhang J, Bonaldo P, Liedtke W, et al. Type VI collagen regulates pericellular matrix properties, chondrocyte swelling, and mechanotransduction in mouse articular cartilage. Arthritis Rheum. 2015;67(5):1286–1294. doi: 10.1002/art.39034.

[27] Du G, Li L, Zhang X, Liu J, Hao J, Zhu J, et al. Roles of TRPV4 and piezo channels in stretch-evoked Ca2+ response in chondrocytes. Exp Biol Med. 2020;245(3):180–189. doi: 10.1177/1535370219892601.

[28] Fu S, Meng H, Inamdar S, Das B, Gupta H, Wang W, et al. Activation of TRPV4 by mechanical, osmotic or pharmaceutical stimulation is anti-inflammatory blocking IL-1β mediated articular cartilage matrix destruction. Osteoarthritis Cartilage. 2021;29(1):89–99. doi: 10.1016/j.joca.2020.08.002.

[29] Servin-Vences MR, Moroni M, Lewin GR, Poole K. Direct measurement of TRPV4 and PIEZO1 activity reveals multiple mechanotransduction pathways in chondrocytes. eLife. 2017;6. doi: 10.7554/eLife.21074.

[30] Nims RJ, Pferdehirt L, Ho NB, Savadipour A, Lorentz J, Sohi S, et al. A synthetic mechanogenetic gene circuit for autonomous drug delivery in engineered tissues. Sci Adv. 2021;7(5):1–36. doi: 10.1126/sciadv.abd9858.

[31] Wyczalkowski MA, Chen Z, Filas BA, Varner VD, Taber LA. Computational models for mechanics of morphogenesis. Birth Defects Res C Embryo Today. 2012;96(2):132–152. doi: 10.1002/bdrc.21013.

[32] Giorgi M, Verbruggen SW, Lacroix D. In silico bone mechanobiology: modeling a multifaceted biological system. Wiley Interdiscip Rev Syst Biol Med. 2016;8(6):485–505. doi: 10.1002/wsbm.1356.

[33] Heegaard JH, Beaupré GS, Carter DR. Mechanically modulated cartilage growth may regulate joint surface morphogenesis. J Orthop Res. 1999;17(4):509–517. doi: 10.1002/jor.1100170408.

[34] Giorgi M, Carriero A, Shefelbine SJ, Nowlan NC. Mechanobiological simulations of prenatal joint morphogenesis. J Biomech. 2014;47(5):989–995. doi: 10.1016/j.jbiomech.2014.01.002.

[35] Giorgi M, Carriero A, Shefelbine SJ, Nowlan NC. Effects of normal and abnormal loading conditions on morphogenesis of the prenatal hip joint: Application to hip dysplasia. J Biomech. 2015;48(12):3390–3397. doi: 10.1016/j.jbiomech.2015.06.002.

[36] Felipe A, Pinzón C, Márquez K, Kraft RH, Ramtani S, Alexander D, et al. Computational model of a synovial joint morphogenesis. Biomech Model Mechanobiol. 2019;(0123456789). doi: 10.1007/s10237-019-01277-4.

[37] Parkkinen JJ, Lammi MJ, Helminen HJ, Tammi M. Local stimulation of proteoglycan synthesis in articular cartilage explants by dynamic compression in vitro. J Orthop Res. 1992;10(5):610–620. doi: 10.1002/jor.1100100503.

[38] Guilak F, Meyer BC, Ratcliffe A, Mow VC. The effects of matrix compression on proteoglycan metabolism in articular cartilage explants. Osteoarthritis Cartilage. 1994;2(2):91–101. doi: 10.1016/S1063-4584(05)80059-7.

[39] Kim YJ, Sah RLY, Grodzinsky AJ, Plaas AHK, Sandy JD. Mechanical regulation of cartilage biosynthetic behavior: Physical stimuli. Arch Biochem Biophys. 1994;311(1):1–12. doi: 10.1006/abbi.1994.1201.

[40] Mouw JK, Imler SM, Levenston ME. Ion-channel regulation of chondrocyte matrix synthesis in 3D culture under static and dynamic compression. Biomech Model Mechanobiol. 2007;6(1-2):33–41. doi: 10.1007/s10237-006-0034-1.

[41] Jeon JE, Schrobback K, Hutmacher DW, Klein TJ. Dynamic compression improves biosynthesis of human zonal chondrocytes from osteoarthritis patients. Osteoarthritis Cartilage. 2012;20(8):906–915. doi: 10.1016/j.joca.2012.04.019.

[42] Gordon-Shaag A, Zagotta WN, Gordon SE. Mechanism of Ca2+-dependent desensitization in TRP channels. Channels. 2008;2(2):125–129. doi: 10.4161/chan.2.2.6026.

[43] Jin M, Wu Z, Chen L, Jaimes J, Collins D, Walters ET, et al. Determinants of TRPV4 activity following selective activation by small molecule agonist GSK1016790A. PLoS ONE. 2011;6(2):e16713. doi: 10.1371/journal.pone.0016713.

[44] Duerr TJ, Comellas E, Jeon EK, Farkas JE, Joetzjer M, Garnier J, et al. 3D Visualization of Macromolecule Synthesis. eLife. 2020;9. doi: 10.7554/elife.60354.

[45] Nilius B, Voets T. The puzzle of TRPV4 channelopathies. EMBO Rep. 2013;14(2):152–63. doi: 10.1038/embor.2012.219.

[46] Rosenbaum T, Benítez-Angeles M, Sánchez-Hernández R, Morales-Lázaro SL, Hiriart M, Morales-Buenrostro LE, et al. Trpv4: A physio and pathophysiologically significant ion channel. Int J Mol Sci. 2020;21(11). doi: 10.3390/ijms21113837.

[47] Doube M, Klosowski MM, Arganda-Carreras I, Cordelières FP, Dougherty RP, Jackson JS, et al. BoneJ: Free and extensible bone image analysis in ImageJ. Bone. 2010;47(6):1076–1079. doi: 10.1016/j.bone.2010.08.023.

[48] Weigert M, Schmidt U, Haase R, Sugawara K, Myers G. Star-convex polyhedra for 3D object detection and segmentation in microscopy. In: IEEE WACV; 2020. p. 3655–3662. doi: 10.1109/WACV45572.2020.9093435.

[49] Bolte S, Cordelières FP. A guided tour into subcellular colocalization analysis in light microscopy. J Microsc. 2006;224(3):213–232. doi: 10.1111/j.1365-2818.2006.01706.x.

[50] Schindelin J, Arganda-Carreras I, Frise E, Kaynig V, Longair M, Pietzsch T, et al. Fiji: An open-source platform for biological-image analysis. Nat Methods. 2012;9(7):676–682. doi: 10.1038/nmeth.2019.

[51] von Chamier L, Laine RF, Jukkala J, Spahn C, Krentzel D, Nehme E, et al. Democratising deep learning for microscopy with ZeroCostDL4Mic. Nat Commun. 2021;12(1):1–18. doi: 10.1038/s41467-021-22518-0.

[52] MATLAB. version 9.7.0.813654 (R2019b). Natick, Massachusetts: The MathWorks Inc.; 2019.

[53] Shapiro F. Pediatric Orthopedic Deformities. vol. 1. Springer International Publishing; 2016. doi: 10.1007/978-3-319-20529-8.

[54] Guilak F, Mow VC. The mechanical environment of the chondrocyte: A biphasic finite element model of cell-matrix interactions in articular cartilage. J Biomech. 2000;33(12):1663–1673. doi: 10.1016/S0021-9290(00)00105-6.

[55] Kim E, Guilak F, Haider MA. The dynamic mechanical environment of the chondrocyte: A biphasic finite element model of cell-matrix interactions under cyclic compressive loading. J Biomech Eng. 2008;130(6). doi: 10.1115/1.2978991.

[56] Lai WM, Hou JS, Mow VC. A triphasic theory for the swelling and deformation behaviors of articular cartilage. J Biomech Eng. 1991;113(3):245–258. doi: 10.1115/1.2894880.

[57] Wilson W, Van Donkelaar CC, Huyghe JM. A Comparison Between Mechano-Electrochemical and Biphasic Swelling Theories for Soft Hydrated Tissues. J Biomech Eng. 2005;127(1):158. doi: 10.1115/1.1835361.

[58] Shefelbine SJ, Carter DR. Mechanobiological predictions of growth front morphology in developmental hip dysplasia. J Orthop Res. 2004;22(2):346–352. doi: 10.1016/j.orthres.2003.08.004.

[59] Arndt D, Bangerth W, Davydov D, Heister T, Heltai L, Kronbichler M, et al. The DEAL.II finite element library: Design, features, and insights. Comput Math Appl. 2020;81:407–422. doi: 10.1016/j.camwa.2020.02.022.

[60] Comellas E, Budday S, Pelteret JP, Holzapfel GA, Steinmann P. Modeling the porous and viscous responses of human brain tissue behavior. Comput Methods Appl Mech Eng. 2020;369:113128. doi: 10.1016/j.cma.2020.113128.

[61] Krupkova O, Zvick J, Wuertz-Kozak K. The role of transient receptor potential channels in joint diseases. Eur Cell Mater. 2017;34:180–201. doi: 10.22203/eCM.v034a12.

[62] Lee W, Leddy HA, Chen Y, Lee SH, Zelenski NA, McNulty AL, et al. Synergy between Piezo1 and Piezo2 channels confers high-strain mechanosensitivity to articular cartilage. Proc Natl Acad Sci U S A. 2014;111(47):E5114–E5122. doi: 10.1073/pnas.1414298111.

[63] Rock MJ, Prenen J, Funari VA, Funari TL, Merriman B, Nelson SF, et al. Gain-of-function mutations in TRPV4 cause autosomal dominant brachyolmia. Nat Genet. 2008;40(8):999–1003. doi: 10.1038/ng.166.

[64] Nishimura G, Lausch E, Savarirayan R, Shiba M, Spranger J, Zabel B, et al. TRPV4-associated skeletal dysplasias. Am J Med Genet C Semin Med Genet. 2012;160 C(3):190–204. doi: 10.1002/ajmg.c.31335.

[65] Wallace H, Maden M. The cell cycle during amphibian limb regeneration. J Cell Sci. 1976;20(3):539–547. doi: 10.1242/jcs.20.3.539.

[66] Costa EC, Otsuki L, Albors AR, Tanaka EM, Chara O. Spatiotemporal control of cell cycle acceleration during axolotl spinal cord regeneration. eLife. 2021;10:1–30. doi: 10.7554/eLife.55665.

[67] Urban JPG, Hall AC. The Effects of Hydrostatic and Osmotic Pressures on Chondrocyte Metabolism. In: Cell Mechanics and Cellular Engineering. Springer New York; 1994. p. 398–419. doi: 10.1007/978-1-4613-8425-0_22.

[68] Browning JA, Saunders K, Urban JPG, Wilkins RJ. The influence and interactions of hydrostatic and osmotic pressures on the intracellular milieu of chondrocytes. Biorheology. 2004;41(3-4):299–308.

[69] Mizuno S, Ogawa R. Using changes in hydrostatic and osmotic pressure to manipulate metabolic function in chondrocytes. Am J Physiol Cell Physiol. 2011;300(6):1234–1245. doi: 10.1152/ajpcell.00309.2010.

[70] Pattappa G, Zellner J, Johnstone B, Docheva D, Angele P. Cells under pressure - the relationship between hydrostatic pressure and mesenchymal stem cell chondrogenesis. Eur Cell Mater. 2019;37:360–381. doi: 10.22203/eCM.v037a22.

[71] Comellas E, Carriero A, Giorgi M, Pereira AF, Shefelbine SJ. Modeling the Influence of Mechanics on Biological Growth. In: Cerrolaza M, Shefelbine S, Garzón-Alvarado D, editors. Numerical Methods and Advanced Simulation in Biomechanics and Biological Processes. 1st ed. Elsevier; 2018. p. 17–35. doi: 10.1016/B978-0-12-811718-7.00002-2.

[72] Stringer C, Wang T, Michaelos M, Pachitariu M. Cellpose: a generalist algorithm for cellular segmentation. Nat Methods. 2021;18(1):100–106. doi: 10.1038/s41592-020-01018-x.

[73] Berteau JP, Oyen M, Shefelbine SJ. Permeability and shear modulus of articular cartilage in growing mice. Biomech Model Mechanobiol. 2016;15(1):205–212. doi: 10.1007/s10237-015-0671-3.

[74] Bennett AF, Garland T, Else PL. Individual correlation of morphology, muscle mechanics, and locomotion in a salamander. Am J Physiol Regul Integr Comp Physiol. 1989;256(6). doi: 10.1152/ajpregu.1989.256.6.r1200.

[75] Tesařová M, Mancini L, Simon A, Adameyko I, Kaucká M, Elewa A, et al. A quantitative analysis of 3D-cell distribution in regenerating muscle-skeletal system with synchrotron X-ray computed microtomography. Sci Rep. 2018;8(1). doi: 10.1038/s41598-018-32459-2.